Diving into the magnetosphere of the Of?p star HD 108

Gregor Rauw [ID],[1]★† Yaël Nazé [ID],[1] Asif ud-Doula [ID][2] and Coralie Neiner [ID][3]

[1]*Space Sciences, Technologies and Astrophysics Research (STAR) Institute, Université de Liège, Allée du 6 Août, 19c, Bât B5c, Liège 4000, Belgium*
[2]*Penn State Scranton, 120 Ridge View Drive, Dunmore, PA 18512, USA*
[3]*LESIA, Paris Observatory, PSL University, CNRS, Sorbonne University, Université de Paris Cité, 5 Place Jules Janssen, Meudon 92195, France*

ABSTRACT

We analyse optical and X-ray spectroscopy of the Of?p star HD 108, known for its strong dipolar magnetic field and its optical line profile variability with a time-scale of 54 ± 3 yrs, interpreted as the stellar rotation period. Optical emission lines have now recovered from their minimum emission state reached in 2007–2008. The variations of the equivalent width of the Hα emission provide constraints on the inclination of the rotation axis (i) and the obliquity of the magnetic axis (β). The best agreement between model and observations is found for (i, β) pairs with $i + \beta \simeq 85°$ and $i \in [30°, 55°]$. The Balmer emission lines display stochastic variability at the $\sim$5 per cent level on time-scales of a few days. *TESS* photometry unveils transient modulations on similar time-scales in addition to prominent red noise variations. A *Chandra* X-ray observation of December 2021, when the star was at a higher emission level, indicates a slight increase of the flux and a spectral hardening compared to the August 2002 *XMM-Newton* observation, taken near minimum emission state. Magnetohydrodynamic simulations are used to compute synthetic X-ray spectra. With our current best estimate of the $\dot{M}_{B=0}$ mass-loss rate, the simulated X-ray luminosity and spectral energy distribution agree very well with the observations. Finally, the radial velocities vary on a period of 8.5 yr with a peak-to-peak amplitude of 10–11 km s^{-1}, suggesting orbital motion with an unseen companion of at least 4 M$_{\odot}$.

Key words: stars: early-type – stars: massive – stars: variables: general – X-rays: stars - stars: individual: HD 108 .

1 INTRODUCTION

Ever since the discovery of HD 108's emission-line spectrum, nearly a century ago (Merrill, Humason & Burwell 1925), the properties and variability of this star have challenged astrophysicists (e.g. Mannino & Humblet 1955; Brucato 1971; Andrillat et al. 1973; Vreux & Conti 1979; Underhill 1994). Extending the pioneering compilation of literature data of Andrillat et al. (1973), Nazé, Vreux & Rauw (2001) presented a long-term spectroscopic monitoring complemented by literature data from over eight decades. They showed that HD 108 undergoes recurrent transitions of its H I and He I lines from absorption to (apparent) P-Cygni profiles and in some cases pure emissions. These authors tentatively suggested a time-scale of variability of 56 yr. They further showed that the apparent P-Cygni like profiles are not genuine P-Cygni profiles, but result instead from a narrow variable emission on top of a photospheric absorption. As a result of the variable emission infilling the He I λ 4471 classification line, the apparent spectral type was found to vary between O 4 in August 1987 and O 7.5 in September 2000 (Nazé et al. 2001). Beside the H I Balmer lines and the He I lines, strong variations were also seen in the Si III $\lambda\lambda$ 4552, 4568, and C III $\lambda\lambda$ 4647-52 emissions. N III $\lambda\lambda$ 4634-41 and He II λ 4686 displayed lower amplitude variations, while O II emissions and the S IV $\lambda\lambda$ 4486, 4504 emissions were only marginally variable.

In parallel, Nazé et al. (2004) presented an *XMM-Newton* observation of HD 108 taken in August 2002. The X-ray spectrum unveiled the signature of two optically thin thermal plasma components with kT near 0.2 and 1.4 keV, and the star was found to be X-ray overluminous compared to normal O-type stars.

In fact, HD 108 belongs to the Of?p category that was originally defined by Walborn (1972, 1973) as Of stars displaying certain peculiarities, among which the presence of strong C III $\lambda\lambda$ 4647–52 emission lines. Over the last two decades, it was found that recurrent line profile variations and X-ray overluminosity are common features of Of?p stars (Nazé, Walborn & Martins 2008b). The three historical members of this class display a wide range of time-scales for their spectral variations: 7.031 d for HD 148 937 (Nazé et al. 2008a), 537.6 d for HD 191 612 (Walborn et al. 2004) and $\sim$55 yr for HD 108. The explanation of these intriguing properties came from the discovery that these stars feature relatively strong dipolar magnetic fields (Donati et al. 2006; Martins et al. 2010; Wade et al. 2012a). Walborn et al. (2010) added two more stars to the Of?p category: NGC 1624-2 and CPD$-$28° 2561 which were subsequently found to also feature strong dipolar magnetic fields, and to display cyclic spectral variations with periods of, respectively, 158 d and 73.4 d (Wade et al. 2012b, 2015).

The properties of Of?p stars are nowadays interpreted in the framework of the oblique magnetic rotator model that was originally proposed for σ Ori E (Shore & Brown 1990) and θ^1 Ori C (Stahl et al. 1996). The magnetic field deflects the stellar winds from both magnetic hemispheres towards the magnetic equator where they collide (Babel & Montmerle 1997; ud-Doula & Owocki 2002, 2022). The ensuing strong shock produces a hot plasma in the post-shock region, which generates the observed X-ray emission (for a review,

★ E-mail: g.rauw@uliege.be
† Senior Research Associate FRS-FNRS (Belgium).

see ud-Doula & Nazé 2016). The shocked plasma subsequently cools, forming a disk-like structure roughly located in the plane of the magnetic equator. As the magnetic field axis is inclined with respect to the rotation axis, the strength of the observed Balmer emission lines is modulated on the stellar rotation period (Sundqvist et al. 2012): the strongest emission is observed when the magnetically-confined wind region is seen face-on and the weakest emission when the confined wind is seen edge-on. The material trapped by the strong dipolar magnetic field also brakes the stellar rotation (ud-Doula, Owocki & Townsend 2009). In this context, HD 108 is the most extreme case known to date as its rotation has been braked to near $0\,\mathrm{km\,s^{-1}}$ (Martins et al. 2010).

In this paper, we present a new set of optical and X-ray observations of HD 108 (Section 2). In Section 3, we use these data to investigate optical variability on various time-scales and to assess the multiplicity of HD 108. The X-ray data of HD 108 are analysed in Section 4. Section 5 describes our efforts to model the magnetosphere of HD 108, and Section 6 summarizes our findings and conclusions.

2 OBSERVATIONS AND DATA PROCESSING

2.1 Spectroscopic monitoring

Since the last report on HD 108's spectral variations by Nazé et al. (2010), we continued monitoring the spectral changes of the star through yearly snapshot observations with the Aurélie spectrograph (Gillet et al. 1994) at the 1.52 m telescope of the Observatoire de Haute Provence (OHP) in France. Our observations used different gratings and covered different wavelength domains. Most of the time we used a $600\,1\,\mathrm{mm^{-1}}$ grating to observe a 430 Å-wide wavelength domain centered at 4670 Å or 6630 Å. Some campaigns rather used a $1200\,1\,\mathrm{mm^{-1}}$ grating to observe a 210 Å-wide domain centred at 4565 Å. Until 2018, the detector was a Charge Coupled Device (CCD) manufactured by the English Electric Valve (EEV) company with 2048×1024 pixels. From 2019 on, it was replaced by an Andor CCD camera with 2048×512 pixels. Both detectors had pixel sizes of $13.5\,\mu\mathrm{m}$ squared. Typical integration times of individual exposures were 15–30 min (depending on the weather conditions). The OHP spectra were reduced using version 17FEBpl 1.2 of the MIDAS software developed at ESO.

From 2013 on, we also monitored HD 108 with the 1.2 m TIGRE telescope (Schmitt et al. 2014; González-Perez et al. 2022) at La Luz Observatory near Guanajuato (Mexico). TIGRE is operated in a fully robotic way and uses the refurbished HEROS echelle spectrograph (Kaufer 1998; Schmitt et al. 2014) which offers a spectral resolving power of 20 000 over the optical range from 3760 to 8700 Å. Most of the time, a single observation was taken per year, but in 2013, 2014, and 2015, we performed more intensive campaigns to investigate the variations on time-scales of several days, up to a few weeks. The TIGRE spectra were reduced with the HEROS reduction pipeline (Mittag et al. 2011; Schmitt et al. 2014).

Finally, we retrieved archival echelle spectra obtained with the NARVAL instrument at the Telescope Bernard Lyot (TBL) and with the ESPaDOnS instrument at the Canada-France-Hawaii Telescope (CFHT). These data are described by Martins et al. (2010) and Shultz & Wade (2017).

For all the spectra covering the regions around the He I λ 5876 and Hα lines, we used the `telluric` tool within IRAF in combination with the atlas of telluric lines of Hinkle et al. (2000) to remove the absorptions due to the Earth's atmosphere. All spectra were continuum-normalized using the MIDAS software adopting best-fit spline functions adjusted to the same set of continuum windows

for all spectra. We further re-analysed all OHP data taken from 1987 on and which were previously discussed by Nazé et al. (2001), Nazé et al. (2004), Nazé et al. (2006), and Nazé et al. (2010). The journal of our observations including the results of some measurements is given in Table A1.

2.2 Photometry

High-cadence space-borne photometry of HD 108 was obtained with the Transiting Exoplanet Survey Satellite (*TESS*, Ricker et al. 2015). *TESS* gathers high-precision photometry in the 6000 Å to $1\,\mu\mathrm{m}$ bandpass. The sky is divided into partially overlapping sectors covering an area of $24° \times 96°$. Each sector is observed for about 27 d, i.e. two consecutive spacecraft orbits separated by a gap around perigee passage. HD 108 was observed with *TESS* camera 3 during sectors 17 and 18 (i.e. between 2019 October 7 and November 27), with camera 3 during sector 57 (2022 September 30 to October 29) and with camera 2 during sector 58 (2022 October 29 to November 26). For sectors 17 and 18, we retrieved the 2-min high-cadence photometric light curves from the Mikulski Archive for Space Telescopes (MAST) portal.[1] The light curves produced by the *TESS* pipeline (Jenkins et al. 2016) provide simple background-corrected aperture photometry and so-called presearch data conditioning (PDC) photometry obtained after removing trends correlated with systematic spacecraft or instrument effects. For our analysis, we focused on the PDC fluxes converted into magnitudes, and we retained only those data points with a quality flag equal to 0. These PDC magnitudes have formal photometric accuracies of 0.26 mmag. For targets with observations over several sectors, the mean PDC magnitudes can differ between consecutive sectors. For our combined analysis, we therefore subtracted the mean magnitude from each sector. For sectors 57 and 58, we extracted aperture photometry light curves at a 200 s cadence using the `Lightkurve`[2] software. The background was evaluated from pixels with fluxes below the median flux. We tested background correction using either the median of the background pixels or performing a principal component analysis (PCA) with five components. Both cases yielded similar light curves, and only those obtained via the PCA technique are presented in the forthcoming sections. As before, the background-corrected fluxes were converted into magnitudes and the mean magnitude of the corresponding sector was subtracted.

The *TESS* CCD detectors have pixels of size $15\,\mu\mathrm{m}$ squared corresponding to $(21\,\mathrm{arcsec})^2$ on the sky. Because the flux of a given source is extracted over apertures of several pixels, source crowding can become an issue. To check whether this is the case here, we searched the *GAIA* early data release 3 catalog (EDR3, Gaia Collaboration et al. 2021) for the magnitudes of sources within a 1 arcmin radius of HD 108. While a large number (99) of objects are located inside this area, the brightest neighbouring source is actually 6.2 mag fainter than HD 108. Therefore, no significant contamination of the *TESS* photometry of HD 108 is expected.

2.3 X-ray observations

The *Chandra* X-ray Observatory (Weisskopf et al. 2000) observed HD 108 on 2021 December 4 (HJD 2459553.178 at mid-exposure) for 15 ks using the ACIS-S instrument (ObsID 25107). To keep photon pile-up as low as possible, only a single ACIS chip (S3) with a 1/8 subarray was used. This set-up yielded a frame time

---

[1] http://mast.stsci.edu/
[2] https://docs.lightkurve.org

of 0.4 s. The observed count rate of the source was $7.7\,10^{-2}\,\mathrm{ct\,s^{-1}}$, which should result in a low pile-up fraction of 1.2 per cent. The corresponding level 2 event file provided by the *Chandra* pipeline was further processed using CIAO v4.14 and CALDB v4.9.6. The source spectrum was extracted with the CIAO task SPECEXTRACT over a circular area of 3.5 arcsec radius centred on the source. The background spectrum was estimated from a surrounding annulus with inner and outer radii of 3.5 and 15.0 arcsec. A weighted response matrix and ancillary response file were generated. The source spectrum was finally binned to reach a minimum of 10 counts per bin.

Previously, HD 108 was observed for 35 ks with *XMM-Newton* (Jansen et al. 2001) on 2002 August 21 (HJD 2452507.864 at mid exposure). A detailed description of this observation is given by Nazé et al. (2004). To account for the most up-to-date status of the calibration of the instruments of *XMM-Newton*, we reprocessed these data with the Science Analysis System software version 18.0.0 and using the current calibration files available in April 2022.

3 OPTICAL VARIABILITY

3.1 *TESS* photometry

The *TESS* photometric time series were analysed with the modified Fourier periodogram algorithm of Heck, Manfroid & Mersch (1985) and Gosset et al. (2001), which explicitly accounts for uneven sampling. With a nominal time step of 2 min, the sectors 17 and 18 time series have a Nyquist frequency of $360\,\mathrm{d^{-1}}$, while it amounts to $216\,\mathrm{d^{-1}}$ for sectors 57 and 58. The periodograms display the highest power at low frequencies, while the periodogram is essentially empty at frequencies above $4\,\mathrm{d^{-1}}$. In the individual periodograms of sectors 17 and 18, the strongest peaks are found, respectively, at $0.162\,\mathrm{d^{-1}}$ and $0.210\,\mathrm{d^{-1}}$ with amplitudes of, respectively, 1.6 mmag and 1.2 mmag. If we combine the data from the two sectors, we find the highest peak at $0.163\,\mathrm{d^{-1}}$ with an amplitude of 1.0 mmag. This agrees well with the 6.16 d signal found independently in the same *TESS* data by Trigueros Páez et al. (2021). On the contrary, no significant individual peak shows up in the periodograms of sectors 57 and 58.

To further investigate the temporal evolution of the frequency content, we computed time-frequency diagrams (Fig. 1) by performing a Fourier analysis of the photometric time series cut into windows of 10 d duration and sliding with a step of 1 d. We see that the frequency content of the periodogram changes with time in an apparently stochastic way. This suggests that a large part of the low-frequency signal is due to a red noise component. The fact that the frequency and morphology of the highest peak change with time during sectors 17 and 18 and that it had disappeared in the sectors 57 and 58 indicates that we are dealing with a transient feature, which could be a fluctuation of the red noise component.

To describe the properties of these stochastic variations, we adopt the formalism of Stanishev et al. (2002) to fit the red noise part of the periodogram:

$$A(\nu) = \frac{A_0}{1 + (2\,\pi\,\tau\,\nu)^\gamma} + C_{\mathrm{white\,noise}} \qquad (1)$$

where $A(\nu)$ is the amplitude (in mmag) at frequency ν in the periodogram built from the observations. The scaling factor A_0, the slope γ, the mean lifetime τ (in days), as well as the level of white noise $C_{\mathrm{white\,noise}}$ (in mmag), were determined from a fit to the power spectrum by means of a Levenberg–Marquardt routine. The corresponding best-fit parameters are given in Table 1.

Red noise is commonly found in the analyses of high-quality space-borne photometry of all kinds of massive stars, including main-sequence OB stars, Be stars, as well as evolved Luminous Blue
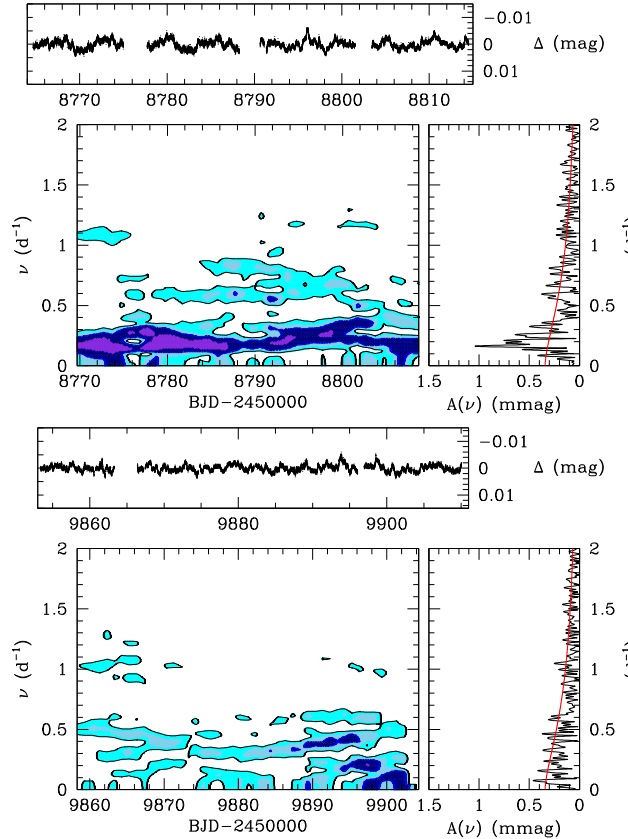
Figure 1. Time-frequency diagrams of the *TESS* photometry of HD 108. The top figure refers to the 2-min PDC photometry of sectors 17 and 18, while the bottom figure stands for the 200 s PCA aperture photometry from sectors 57 and 58. For each figure, the observed light curve is reproduced in the top panel. The bottom left panel provides the evolution of the Fourier periodogram with the date in the *x*-axis corresponding to the middle of the 10-d sliding window. The violet, dark blue, light blue, and cyan colours indicate, respectively, amplitudes ≥ 1.5 mmag, ≥ 1.0 mmag, ≥ 0.75 mmag, and ≥ 0.5 mmag. The right vertical panel illustrates the Fourier periodogram evaluated from the full data set of sectors 17 and 18 (top figure) and sectors 57 and 58 (bottom figure). The red curve yields our best-fit red noise relation computed from equation (1) for sectors 17 and 18.

Table 1. Red noise properties of the periodogram of the sectors 17 and 18 *TESS* photometry of HD 108.

A_0 (mmag)	0.338 ± 0.004
τ (d)	0.206 ± 0.004
γ	1.58 ± 0.03
$C_{\mathrm{white\,noise}}$ (mmag)	0.0042 ± 0.0004

Variables and Wolf-Rayet stars (e.g. Blomme et al. 2011; Aerts et al. 2017; Ramiaramanantsoa et al. 2018; Bowman et al. 2019, 2020; Nazé, Rauw & Pigulski 2020; Nazé, Rauw & Gosset 2021; Rauw & Nazé 2021). The red noise variability is thought to arise either from convection in a subsurface convection layer (Cantiello et al. 2009, 2021; Grassitelli et al. 2015; Lecoanet et al. 2019) or from gravity waves generated in the convective core of the massive star (Rogers et al. 2013; Aerts & Rogers 2015; Bowman et al. 2019, 2020). The same mechanism is thought to be responsible for the velocity fields that cause macroturbulent broadening of the spectral lines of many massive stars (Cantiello et al. 2021, and references therein).

The detection of a significant red noise variability in the photometry of HD 108 is in line with the value of the macroturbulence
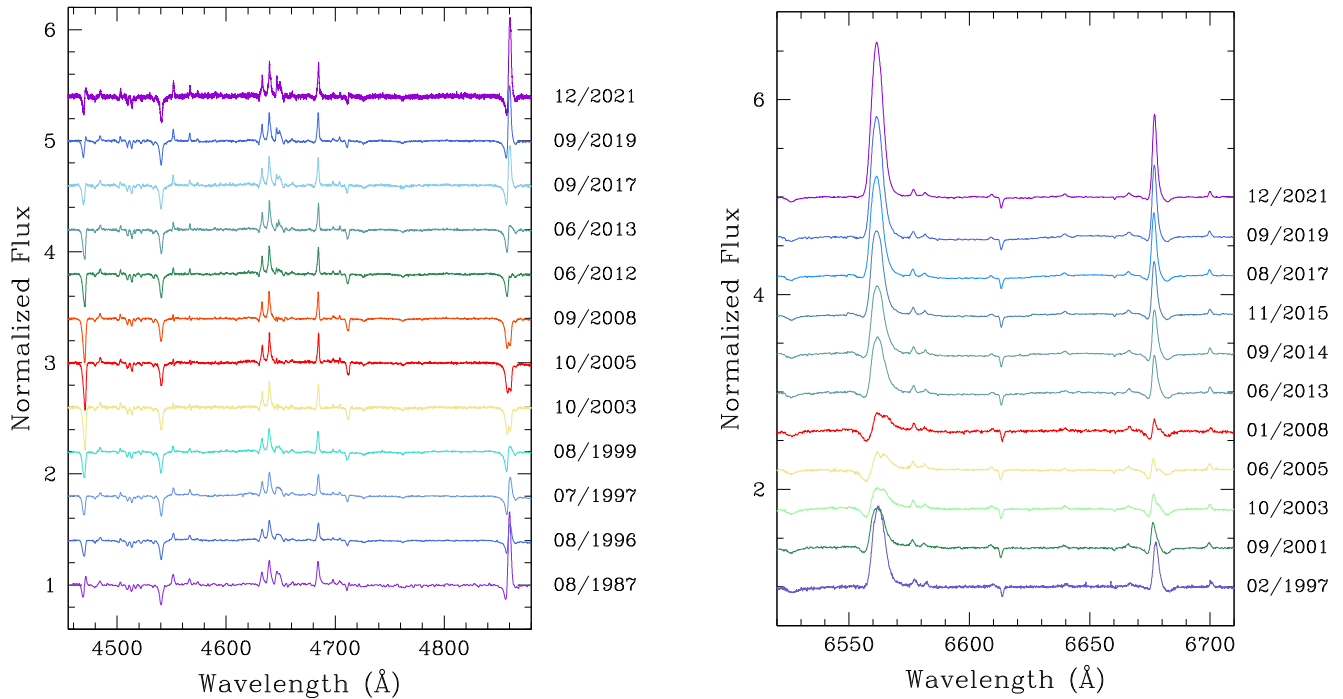
Figure 2. Long-term evolution of the blue (left) and red (right) spectrum of HD 108.
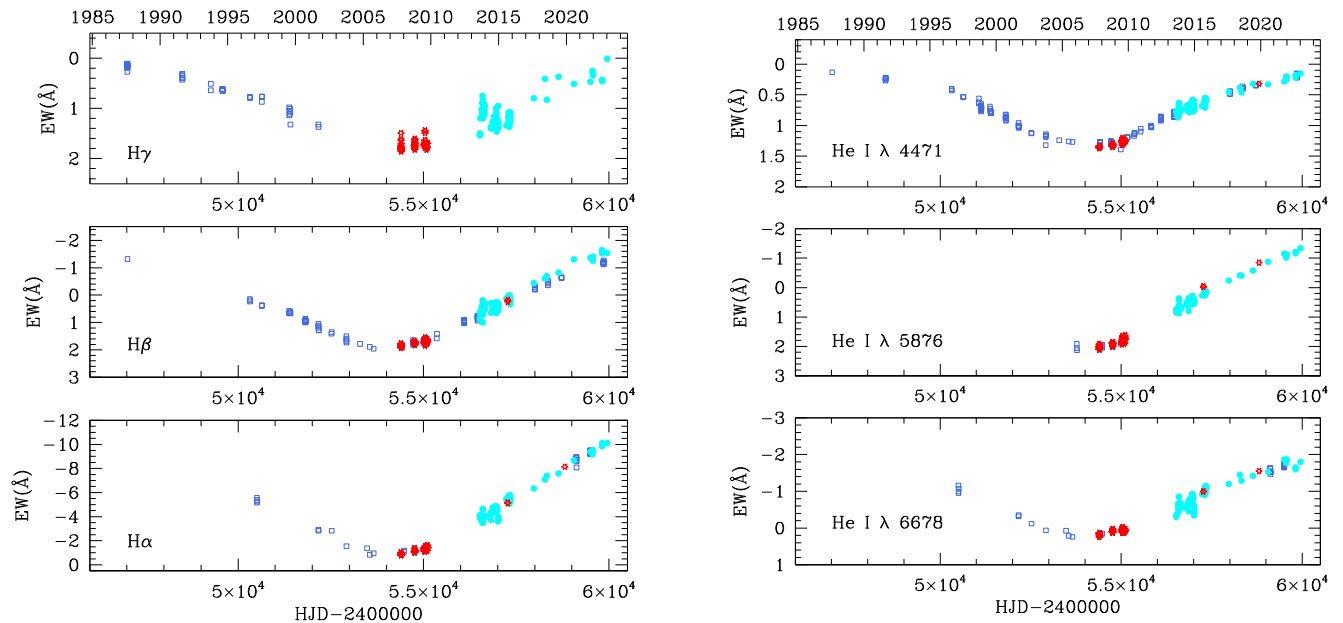
Figure 3. Long-term variations of the EWs of H I (left) and He I lines (right) in the spectrum of HD 108. Different symbols stand for data from different observatories: blue open squares indicate OHP data, red stars are data from the NARVAL (TBL) or ESPaDOnS (CFHT) instruments, while the cyan circles stand for TIGRE data. The horizontal axes are in heliocentric Julian dates, except for the top horizontal axes on each side which is expressed in calendar years.

($64.4 \pm 0.4 \, \mathrm{km \, s^{-1}}$) inferred by Sundqvist et al. (2013). Such a high value of macroturbulence is required to explain the line widths in the absence of significant rotational broadening. While strong magnetic fields could in principle prevent such turbulent motion, Sundqvist et al. (2013) showed that the magnetic fields of Of?p stars, with the exception of NGC 1624-2, are not sufficient to inhibit convective motion inside the subsurface convective layer (see also MacDonald & Petit 2019).

3.2 Long-term spectroscopic variations

The strength of the emission lines in the spectrum of HD 108 reached its minimum around 2007 (Nazé et al. 2010). Since then, the intensity of the emissions has progressively increased, reaching in the years 2021 and 2022 the level previously observed in the early 1990s (see Figs 2 and 3).

Over the part of the cycle covered by our data, the spectrum of HD 108 between 4450 and 4900 Å displays strong variations mostly
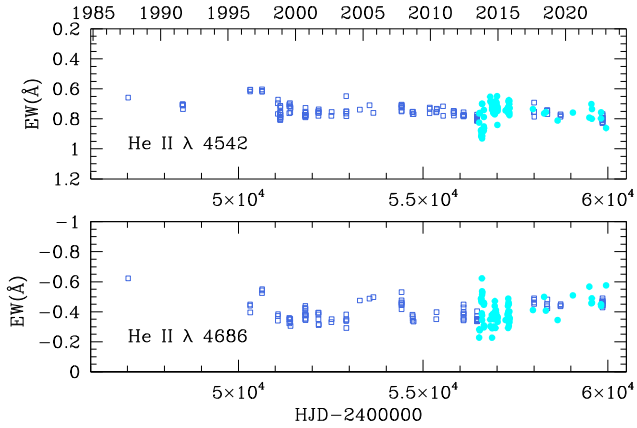
Figure 4. EW of the He II λ 4542 absorption (top panel) and the He II λ 4686 emission (bottom panel) lines in the spectrum of HD 108 as a function of time.

in Hβ, He I λλ 4471, 4713 and the C III emission around 4650 Å (see the left panel of Figs 2 and 3). Lower level variability is also present in the emission of the Si III λλ 4552, 4568, 4575 triplet. Quite remarkably, the Si III λλ 4552, 4568, 4575 lines display an inverse P-Cygni-like profile in the years between 2003 and 2008, i.e. near minimum emission state. The variations of the Hβ line and of the He I lines mostly stem from changes of the narrow emission component superimposed on the photospheric absorption (Nazé et al. 2008b). On the contrary, the He II λ 4542 and N III λλ 4511–4535 absorptions as well as the He II λ 4686 and N III λλ 4634-42 emissions display essentially constant line profiles (see Figs 2 and 4). The lack of strong variability of He II λ 4686 contrasts with the case of HD 191612 where the strength of this emission is clearly variable (Walborn et al. 2004). Comparing HD 108 and HD 191612, we further note that the He I λ 4471 line in the spectrum of HD 191612 does not display an emission component above the continuum even at maximum emission strength, while such an emission component is seen in HD 108 in 1987 as well as in the 2021, 2022, and 2023 spectra. Also, the Hβ emission of HD 108 is significantly stronger at maximum than in the case of HD 191612, and at the time of minimum emission strength, some residual emission remains present in the Hβ line of HD 108, while none is seen in HD 191612.

Very similar remarks apply to the comparison between the variations of the Hα and He I λ 6678 lines in HD 108 (see the right panel of Figs 2 and 3) and HD 191612. For example, while the Hα line goes into absorption during minimum state in HD 191612, the line remains in emission in the minimum state spectrum of HD 108.

The variable emission lines grow in intensity, but are rather narrow features. For instance, the full width at half maximum (FWHM) of the Hα emission component in the 2022 spectra amounts to 5.3 Å, corresponding to 245 km s^{-1}. We measured the equivalent widths (EWs) of the most frequently observed variable lines by integrating the continuum-normalized spectra between specific boundaries. For the Hγ, Hβ, and Hα lines, we, respectively, used the wavelength intervals [4320 Å, 4350 Å], [4845 Å, 4875 Å], and [6550 Å, 6575 Å]. For the He I lines at λ 4471, λ 5876, and λ 6678, we, respectively, used [4465 Å, 4475 Å], [5866 Å, 5881 Å], and [6664 Å, 6694 Å]. We further measured the EWs of the less variable He II λ 4542 absorption and He II λ 4686 emission by integrating over the wavelength intervals [4535.6 Å, 4547.9 Å] and [4680.2 Å, 4690.3 Å]. The results are illustrated in Figs 3 and 4. For the He II lines, we confirm the absence of a well-defined variability with EW(He II λ 4542) = 0.75 ± 0.05 Å, and EW(He II λ 4686) = 0.40 ± 0.07 Å, with
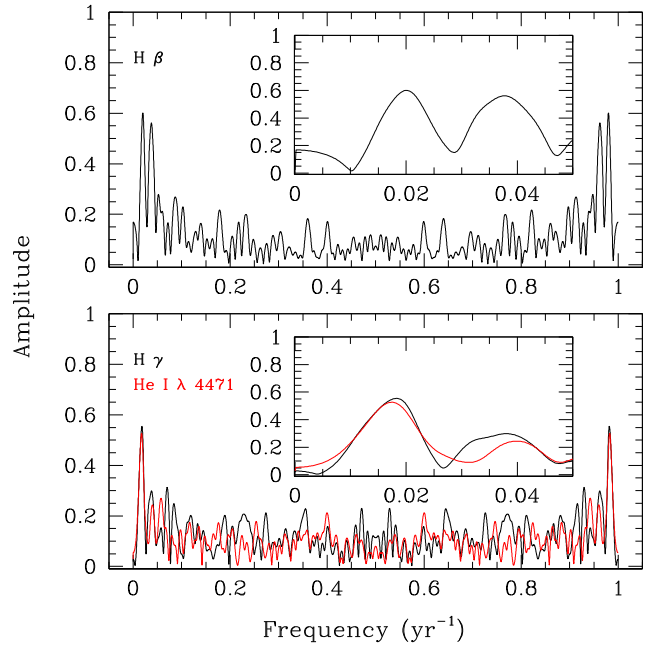
Figure 5. Fourier spectra of the qualitative line profile nature of the Hβ (top panel), Hγ (bottom panel, black), and He I λ 4471 (bottom panel, red) lines in the spectrum of HD 108. The inserts show a zoom on the low-frequency part of the Fourier spectra.

the quoted standard deviation corresponding to the scatter of our full sets of data. For the variable emission lines, if we consider measurements taken over the same night or consecutive nights, we estimate that the typical standard deviation on the EWs amounts to about 5 per cent of their value. This value is of the same order as the observed dispersion of the He II lines. It accounts not only for the measurement uncertainties (typically about 2 per cent of the EW value as estimated from observations taken within less than 1 h of each other), but also includes the contribution of genuine short-term variations (see Section 3.3).

To re-assess the duration of the long emission cycle of HD 108, we combined the compilations of archival data of Brucato (1971), Andrillat et al. (1973), Nazé et al. (2001), and Nazé et al. (2006) with our new data. This yields a time series spanning from 1919 until 2022. We used the following scheme to convert qualitative information on the nature of the line profiles from the oldest references into quantitative data: epochs when a line was observed in strong absorption were assigned a numerical value of −1, dates when the line was seen as an apparent P-Cygni profile were given a value of 0, and epochs when the line was in net emission were assigned a value +1. Some intermediate values were assigned based on the details of the line description in the original reference. We then applied the Fourier method for uneven sampling of Heck et al. (1985) and Gosset et al. (2001) to this time series. The most extensive time series are those for the Hγ, Hβ, and He I λ 4471 lines. The resulting periodograms are illustrated in Fig. 5.

The strongest peaks are found at 0.0200, 0.0182, 0.0174 yr^{-1} for the Hβ, Hγ, and He I λ 4471 lines, respectively. Therefore, our current best value for the duration of the long cycle of HD 108 is 54 ± 3 yr, in good agreement with previous determinations (Nazé et al. 2001; Nazé et al. 2010). For the time of minimum emission line strength (defined as phase $\phi = 0.5$), we obtain a best estimate of HJD 2454284.5. Folding our EW measurements with this period, it is interesting to note that this suggests that, unlike HD 191612,
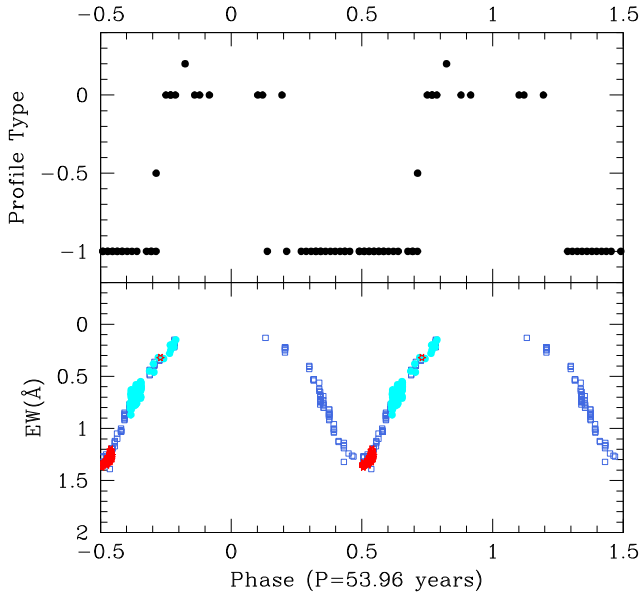
Figure 6. Phase-folded variations of the He I λ 4471 line in the spectrum of HD 108. The top panel illustrates the variations of the qualitative line profile nature as estimated from literature data. The bottom panel displays our own measurements of the EW of the line. Phase $\phi = 0.5$ (i.e. minimum emission) corresponds to HJD 2454284.5.

HD 108 spends more time near the emission maximum than near the minimum. Indeed, while the EW(Hα) variations of HD 191 612 reveal an extended flat minimum that lasts for about one third of its cycle, and a more sharply peaked maximum (Howarth et al. 2007), the existing data on HD 108 rather suggest the opposite situation [i.e. a sharply peaked minimum, with a duration below 5 yr (or < 10 per cent of the cycle) and an extended (flat) maximum, see Fig. 6]. In the oblique magnetic rotator model, these different behaviours most likely stem from different values of the inclination angle of the stellar rotation axes and different values of the obliquity of the magnetic axes (see Section 5.1).

Although we lack a continuous photometric monitoring of HD 108 over its full cycle, it seems likely that the spectral changes go along with brightness changes. Indeed, Barannikov (2007) reported a roughly constant optical brightness between 1989 and 1994. In the following years, the brightness declined until at least 2006 (i.e. the last epoch covered by these observations), which coincides with the epoch of the minimum emission state.

3.3 Short-term spectroscopic variations

Martins et al. (2010) noted the presence of short-term spectroscopic variability mostly in the red part of the He I and wind-sensitive line profiles. On the contrary, photospheric He II lines were found to be very stable. Martins et al. (2010) interpreted these changes as evidence for the infall of material from the magnetosphere, a consequence of dynamical phenomena within the magnetically channeled winds (ud-Doula et al. 2013).

To investigate the properties of such variations, we performed a more intensive spectroscopic monitoring with TIGRE in 2013, 2014, and 2015. Table 2 provides an overview of the data collected during these campaigns. We focus here on the Hα emission line as it offers an efficient diagnostic of the cool plasma in the magnetosphere.

Our data reveal that the level of variability of EW(Hα) is quite similar from one epoch to the other despite the varying overall line

Table 2. Main properties of the more intensive TIGRE monitoring.

| Year	N	$<S/N>$	Δt (days)	EW(Hα) (Å)	$\nu_{peak,\,1}$ (d^{-1})	$\nu_{peak,\,2}$ (d^{-1})
2013	17	299	132	-3.55 ± 0.23	0.033	0.138
2014	20	351	45	-4.23 ± 0.22	0.178	0.158
2015	23	344	52	-5.09 ± 0.19	0.301	0.116

Note. N is the number of spectra taken, $<S/N>$ their mean signal-to-noise ratio evaluated in a line free region between 6757 and 6767 Å, and Δt the time interval of our observations. The fifth column indicates the mean EW(Hα) evaluated between 6550 and 6575 Å, and its dispersion about the mean. The last two columns yield the frequencies of the highest and the second-highest peaks in the associated Fourier power spectra.

strength (see column 5 of Table 2). The scatter is typically of about 0.2 Å, corresponding to about 5 per cent of the emission EW of the Hα line.

Fig. 7 illustrates the temporal variance spectrum (TVS, Fullerton, Gies & Bolton 1996) of the corresponding time series of spectra. The level of variability of the Hα line (above the noise level) typically peaks at about 2 per cent of the continuum. Significant variability is restricted to a relatively narrow wavelength range, from 6555 to 6567 Å. We used the modified Fourier periodogram algorithm of Heck et al. (1985) and Gosset et al. (2001) over this wavelength interval to identify the dominant frequencies in these short-term spectroscopic variations. In general, our Fourier periodograms lack a clearly dominant frequency, but rather consist of a number of peaks with relatively similar amplitudes. The last two columns of Table 2 list the frequencies associated with the strongest peaks in the power spectra of the time series of the different epochs. The two highest peaks in the 2013 Fourier spectrum have a power 6.7 and 4.7 times higher than the noise level. For the 2014 and 2015 data, the power of the highest peak reaches 3.0 times the noise level, whereas the second highest peak reaches 2.5 and 2.0 times the noise level, respectively, in 2014 and 2015. The highest peak in the 2013 Fourier spectrum occurs at a rather low frequency which likely stems from the long-term variations of the Hα line strength and the fact that the 2013 data are spread over nearly 5 months. Within the $0–1\,d^{-1}$ frequency interval, the second-highest peak of the 2013 periodogram occurs at $0.138\,d^{-1}$. The 2014 and 2015 time series were taken over about 1.5 month making them less sensitive to the long-term variations. The strongest peaks in their Fourier spectra are found between 0.116 and $0.301\,d^{-1}$. While some of these frequencies are relatively close to the transient signal found in the sectors 17 and 18 *TESS* photometry; none of them matches exactly with the photometric frequency. Moreover, none of the spectroscopic frequencies appears to be stable from one epoch to the other. We thus conclude that these frequencies likely reflect the recurrence of quasi-cyclic variations, occuring on time-scales of a few days to about a week, rather than genuine periodicities.

3.4 Radial velocities

Binarity with very different periods has been suggested by a number of authors. Hutchings (1975) and Aslanov & Barannikov (1989) proposed rather short orbital periods of 4.6 and 5.8 d, respectively. Such short periods were ruled out by Nazé et al. (2001) based on intense short-term radial velocity (RV) monitorings. Barannikov (1999) claimed the detection of periodic RV variations with a period of 1627.6 d, $K = 10.5\,km\,s^{-1}$, and $e = 0.43$. This result could not be confirmed though (Nazé et al. 2001). Nazé et al. (2001); Nazé et al. (2006); and Nazé et al. (2010) reported RV variations on time-scales of several thousand days. Based on data collected over 18 yr,
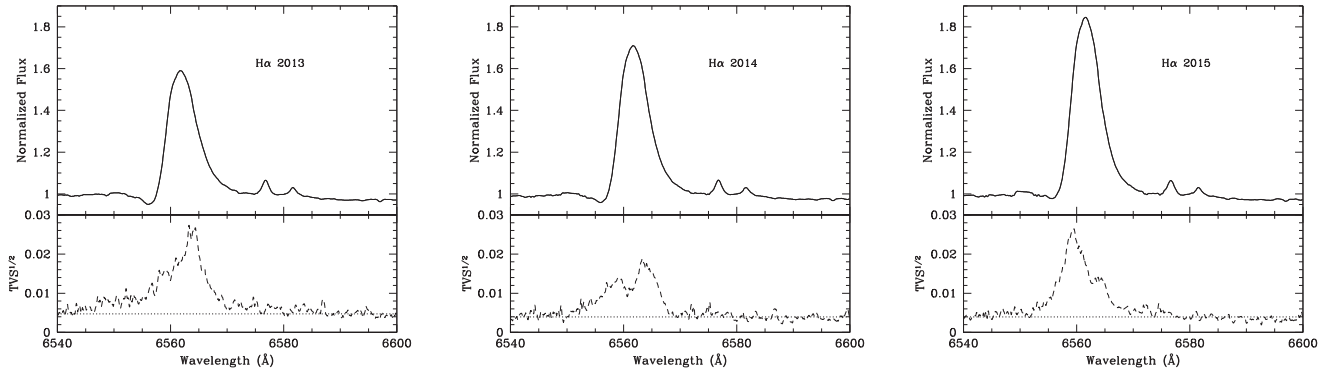
Figure 7. Normalized mean spectrum (top panels) and TVS$^{1/2}$ (bottom panels) of the spectroscopic time series from 2013 (left column), 2014 (middle column), and 2015 (right column). The short-dashed horizontal lines in the bottom panels correspond to the 99 per cent significance level of variability estimated from the S/N ratios of our spectra following the method of Fullerton et al. (1996).

Trigueros Páez et al. (2021) discarded binarity of HD 108. Yet, their data (e.g. their Fig. 10) did show RV variations over a range of about 10–15 km s^{-1}. These authors attributed them to pulsational activity.

We decided to revisit this issue taking advantage of the large data set at our disposal. We measured the RVs of a number of absorption and emission lines in the spectrum of HD 108. We focused on lines that do not display profile variations due to the long-term cycle. We thus measured RVs of the He II λλ 4200, 4542, N III λλ 4511–4535, O III λ 5592 absorption lines and of the He II λ 4686 and C III λ 5696 emission lines. For the He II, O III ,and C III lines, we fitted Gaussian profiles to the lower (resp. upper) 2/3 of the absorption (resp. emission) line. For the N III lines, we instead performed a cross-correlation between the observed spectra and the 4500–4538 Å spectral region in a synthetic TLUSTY spectrum[3] (Lanz & Hubeny 2003). The RVs were then estimated by fitting a parabola to the peak of the correlation function (Verschueren & David 1999).

The RVs of the He II lines reveal at least three cycles of a $\sim$10 km s^{-1} modulation on a time-scale close to 3000 d. We searched for periodicities among the most densely sampled time series of RVs using the same Fourier method as above (see Fig. 8). In this way, we obtained periods of 3194 ± 98 d for He II λ 4542, 3114 ± 94 d for He II λ 4686, and 3076 ± 90 d for N III λλ 4511–4535. Within their errors, these periods agree. We note that the RV data of Trigueros Páez et al. (2021) agree quite well with ours (see Fig. 9).

We note that the dispersion of the RVs measured on observations taken over time-scales of hours and days (i.e. the typical time-scales of pulsations in massive stars) is significantly smaller (σ_{RV} between 0.4 and 1.7 km s^{-1} depending on the spectral resolution of the data) than the $\sim$10 km s^{-1} amplitudes measured above. A periodicity of order 3000 d is unlikely to be associated with pulsations in a massive near main-sequence star. Moreover, since the spectral lines selected for the RV measurements do not display line profile variations related to the long-term rotational cycle, we can safely exclude a connection between the two phenomena. Finally, we stress that lines from different ions, either in absorption or emission, display the same RV variations (both in phase and amplitude). Therefore, the most likely explanation for these periodic RV variations is binarity. We thus applied the Liège Orbital Solution Package (LOSP, Sana, Gosset & Rauw 2006) to establish an SB1 orbital solution. We tested both circular and eccentric orbital solutions. For each line, we found

---

[3]For the TLUSTY template spectrum, we adopted $T_{eff} = 35\,000$ K and $\log g = 3.5$.
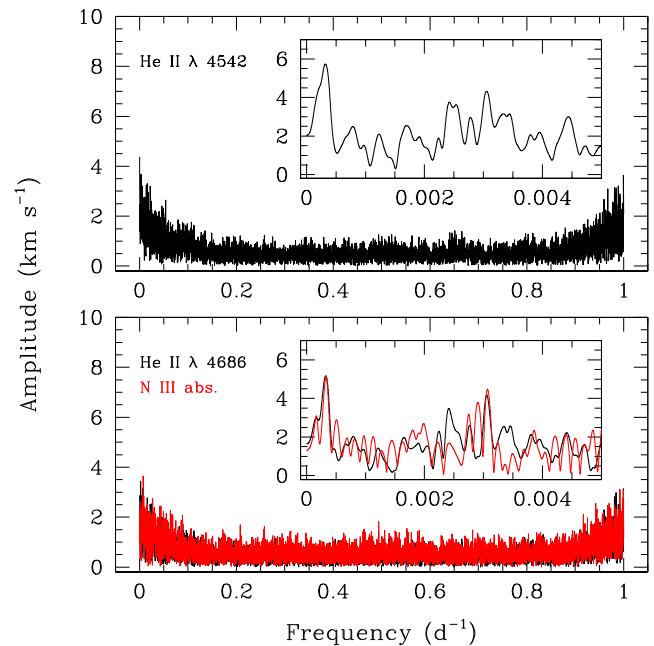
Figure 8. Fourier periodograms of the RVs of the He II λ 4542 absorption (top panel), the He II λ 4686 emission (bottom panel, black), and the N III λλ 4511–4535 absorptions (bottom panel, red) in the spectrum of HD 108. The inserts zoom on the low-frequency part of the Fourier spectra, revealing in each case a dominant peak near 3.2 10^{-4} d^{-1}.

that the eccentric solution did not improve the quality of the fits and that best-fit eccentricities were small and, for the N III lines, only marginally significant. Moreover, different lines yielded discrepant values of e (e.g. $e = 0.12 \pm 0.03$ for He II λ 4542 and $e = 0.16 \pm 0.03$ for He II λ 4686 versus $e = 0.06 \pm 0.06$ for the N III λλ 4511–4535 lines) as well as of the longitude and time of periastron passage. We thus decided to focus on the solutions obtained assuming $e = 0$. The results are listed in Table 3 and the best-fit orbital solution for the RVs of the He II λ 4542 line is shown in Fig. 9. Our present study thus confirms earlier reports by Nazé et al. (2010) and strongly suggests that HD 108 is a binary system with an orbital period near 8.5 yr, and a relatively low eccentricity.

Fig. 10 illustrates the observational constraints on the mass of the secondary component. The mass of the Of?p star was estimated to be $48.8^{+5.4}_{-8.6}$ M$_\odot$ by Martins et al. (2012) from comparison with
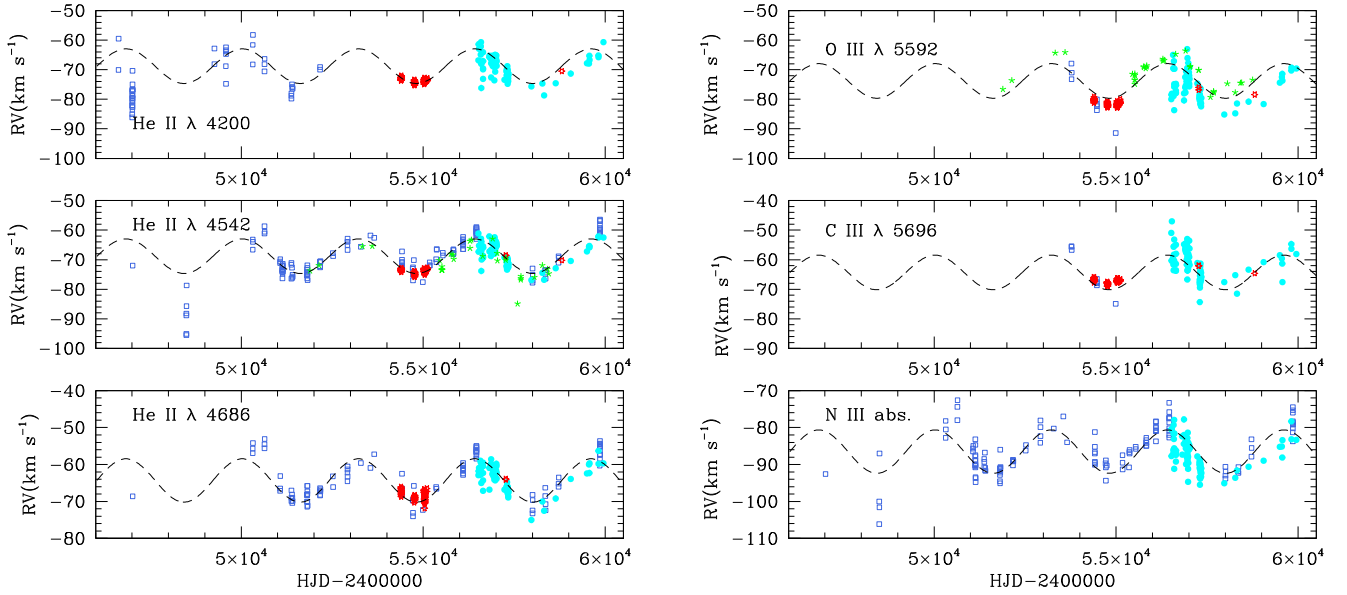
Figure 9. Left: RVs of the He II lines in the spectrum of HD 108. Different symbols refer to data from different observatories: blue open squares indicate data from OHP, red stars stand for NARVAL (TBL) or ESPaDOnS (CFHT) spectra, cyan dots correspond to TIGRE spectra, and green stars indicate RVs listed by Trigueros Páez et al. (2021). The dashed line yields the best-fit SB1 orbital solution of the He II λ 4542 line, shifted to the systemic velocity of the corresponding line. Right: same for several other absorption and emission lines.

evolutionary tracks. However, these authors adopted a distance of 2.51 kpc, which has since then be revised to (1.91 ± 0.11) kpc by Bailer-Jones et al. (2021). This lower distance results in a downwards revision of the evolutionary mass to $38.5 \pm 4\,M_\odot$ (see also Section 5).

From Fig. 10, we then find that the companion must have a mass larger than $\sim 4\,M_\odot$ which rules out the possibility of a white dwarf or neutron star compact companion. We further see that for orbital inclinations larger than $30°$, the mass of the companion is unlikely to exceed $\sim 12\,M_\odot$. Hence, assuming a main-sequence luminosity class, the secondary star's spectral type is most likely in the range B1–B5.

Spectral disentangling can in principle be used to unveil the spectrum of an unseen secondary component in an SB1 binary system (e.g. Mahy et al. 2022). We attempted to do so for HD 108 by applying our spectral disentangling code based on the method of González & Levato (2006) to the Aurélie spectra between 4460 and 4700 Å, i.e. over the most frequently observed spectral domain. We tested values of q between 0.1 and 0.5. Unfortunately, the variable emission features of the Of?p star generate strong artefacts in the secondary spectrum around each variable line that prevent us from unambiguously detecting any secondary spectral feature.

To limit the impact of the long-term variability, we thus repeated the disentangling restricting the input data set to 27 Aurélie spectra taken between 2001 and 2008, i.e. closest to the minimum emission state. Yet, whilst this attenuated the artefacts, the reconstructed secondary spectra for different values of q are still dominated by residuals of the Of?p star spectrum. Hence, at this stage, we have not been able to detect a spectral signature of the secondary star.

While few magnetic stars have been found in close (<30 d) interacting or post-interaction O-star binaries (e.g. Nazé et al. 2015b), the presence of distant companions is not unusual. Amongst the Of?p stars, HD 191 612 has an orbital period of about 1542 d, while its rotational period is 537.6 d. The orbit of HD 191 612 is quite eccentric ($e = 0.44 \pm 0.04$) and the companion is likely an early B-type star (Howarth et al. 2007). As for the latter star, and contrary to HD 108, the third 'historical' Of?p star, HD 148 937, also has an orbital period longer than its rotation period, but the difference is even more extreme with respective values of 18–26 yrs and 7 d (Wade et al. 2019). The orbit of HD 148 937 is also quite eccentric ($e = 0.6-0.8$) and the companion appears to be an O-type star, about 1.5 times more massive than the magnetic Of?p star. The orbit of HD 108 thus appears quite different from those of the other two stars.

Table 3. SB1 orbital solutions of HD 108. T_0 stands for the time of conjunction with the Of?p primary star in front, while v_0 corresponds to the apparent systemic velocity. K_1 and a_1 are the velocity amplitude and semi-major axis of the Of?p primary star. The mass function is equal to $f(m) = \frac{m_2^3 \sin^3 i}{(m_1+m_2)^2}$.

	He II λ 4542	He II λ 4686	N III λλ 4511–4535
$P_{\rm orb}$ (d)	3194	3116	3072
T_0 ($HJD - 2450\,000$)	8808.9 ± 18.5	8770.4 ± 21.7	8612.8 ± 29.0
v_0 (km s^{-1})	-68.8 ± 0.1	-64.3 ± 0.1	-86.5 ± 0.3
K_1 (km s^{-1})	5.9 ± 0.2	5.2 ± 0.2	5.8 ± 0.5
$a_1 \sin i$ (R$_\odot$)	369.7 ± 11.7	321.8 ± 10.9	349.4 ± 27.3
$f(m)$ (M$_\odot$)	0.067 ± 0.006	0.046 ± 0.005	0.061 ± 0.014
r.m.s. (km s^{-1})	2.17	2.17	3.35
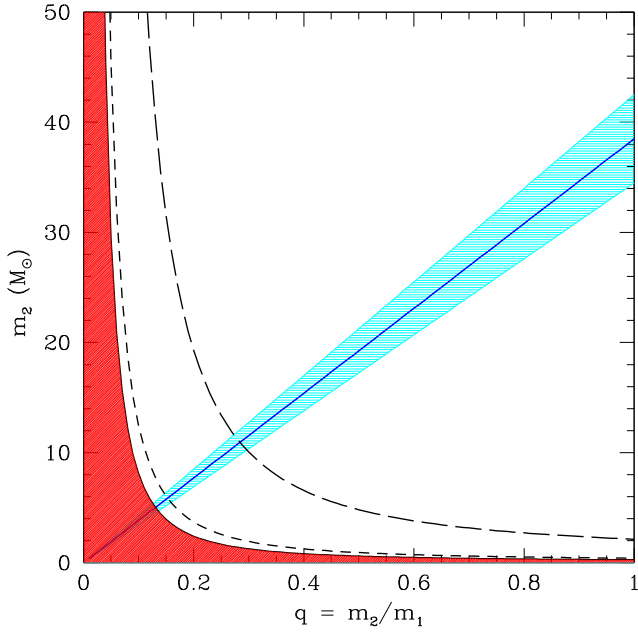
Figure 10. Constraints on the mass of the companion of HD 108. The straight blue line corresponds to the companion mass computed as $m_2 = q \, m_1$ with m_1 the mass of the Of?p star taken to be $m_1 = 38.5 \pm 4 \, M_\odot$ (see text). The light blue hatched area corresponds to the uncertainty on the mass of the Of?p star. The black curves stand for the companion mass computed from the mass function $m_2 = \frac{f(m)(1+1/q)^2}{\sin^3 i}$ with $f(m) = 0.067 \, M_\odot$. The continuous, short-dashed, and long-dashed lines correspond, respectively, to $i = 90°$, $i = 60°$, and $i = 30°$. The red hatched area is a forbidden region in this parameter space.

4 X-RAY EMISSION

Magnetically confined winds of early-type stars are expected to produce a bright and relatively hard X-ray emission (see ud-Doula & Nazé 2016, and references therein). Nazé et al. (2014) found the X-ray luminosity of magnetic massive stars to be strongly correlated with the stellar wind mass-loss rate, with a power–law form that is slightly steeper than linear for the less luminous, lower mass-loss rate B-type stars and flattens for the more luminous, higher mass-loss rate O-type stars. As these winds are radiatively driven, these scalings can be equivalently expressed as relations with the bolometric luminosity. The observed X-ray luminosities, and their trend with mass-loss rates, were found to be well reproduced by magnetohydrodynamic (MHD) models, except for a a few overluminous B-type stars which were mostly rapidly rotating objects (Nazé et al. 2014). In this section, we revisit the X-ray properties of HD 108 to see how it fits into the global picture of magnetic massive stars.

We fitted the archival *XMM-Newton*-EPIC and RGS spectra and the new *Chandra*-ACIS spectrum with xspec version 12.9.0i. The data from both satellites were modeled using a model of the kind phabs$_{\rm ISM}$ * (phabs$_1$ * apec(kT$_1$) + phabs$_2$ * apec(kT$_2$)) where phabs$_{\rm ISM}$ stands for the photoelectric absorption by the interstellar medium (for which we adopted a neutral hydrogen column density of $0.34 \, 10^{22}$ cm^{-2}, Diplas & Savage 1994), while the other phabs components are meant to represent photoelectric absorption by the circumstellar environment (i.e. the stellar wind and/or the magnetosphere). The apec models represent the X-ray emission of a collisionally-ionized optically thin thermal plasma (Smith et al. 2001) with solar abundances taken from Asplund et al. (2009). The results of these fits are described in Table 4. The

Table 4. Results of the fits of the X-ray spectra of HD 108.

	XMM-Newton	*Chandra*
Date (HJD - 2450 000)	2507.864	9553.178
Phase (rot.)	0.41	0.77
Phase (bin.)	0.03	0.23
$N_{\rm H, ISM}$ (10^{22} cm^{-2})	0.34 (fixed)	0.34 (fixed)
	Solar abundances	
$N_{\rm H, 1}$ (10^{22} cm^{-2})	$0.46^{+.08}_{-.05}$	$0.15^{+.25}_{-.15}$
kT_1 (keV)	$0.28^{+.01}_{-.03}$	$0.77^{+.20}_{-.51}$
norm$_1$ (10^{-3} cm^{-5})	$3.0^{+1.6}_{-0.6}$	$0.45^{+.30}_{-.19}$
$N_{\rm H, 2}$ (10^{22} cm^{-2})	$0.64^{+.22}_{-.21}$	$0.33^{+.60}_{-.33}$
kT_2 (keV)	$1.86^{+.14}_{-.12}$	$2.06^{+.93}_{-.40}$
norm$_2$ (10^{-3} cm^{-5})	$0.56^{+.11}_{-.05}$	$0.60^{+.16}_{-.22}$
$f_{\rm X}$ (10^{-13} erg cm^{-2} s^{-1})	6.46 ± 0.04	8.18 ± 0.04
$f_{\rm X}^{\rm un}$ (10^{-13} erg cm^{-2} s^{-1})	11.23	12.54
χ_n^2 (d.o.f.)	1.50 (569)	0.99 (76)
	CNO from Martins et al. (2015)	
$N_{\rm H, 1}$ (10^{22} cm^{-2})	$0.44^{+.04}_{-.04}$	$0.15^{+.25}_{-.15}$
kT_1 (keV)	$0.24^{+.01}_{-.01}$	$0.77^{+.20}_{-.46}$
norm$_1$ (10^{-3} cm^{-5})	$4.6^{+1.0}_{-0.8}$	$0.46^{+.30}_{-.19}$
$N_{\rm H, 2}$ (10^{22} cm^{-2})	$0.76^{+.14}_{-.12}$	$0.34^{+.59}_{-.34}$
kT_2 (keV)	$1.61^{+.07}_{-.07}$	$2.06^{+.86}_{-.40}$
norm$_2$ (10^{-3} cm^{-5})	$0.66^{+.05}_{-.04}$	$0.61^{+.20}_{-.23}$
$f_{\rm X}$ (10^{-13} erg cm^{-2} s^{-1})	6.40 ± 0.04	8.18 ± 0.04
$f_{\rm X}^{\rm un}$ (10^{-13} erg cm^{-2} s^{-1})	11.43	12.54
χ_n^2 (d.o.f.)	1.35 (569)	0.92 (76)

Note. The upper part of the table yields the best-fit results assuming solar abundances, while the lower part quotes the results adopting the CNO abundances of Martins et al. (2015). The $f_{\rm X}$ and $f_{\rm X}^{\rm un}$ values are, respectively, the observed fluxes and the fluxes corrected for absorption by the interstellar medium, both in the 0.5–10 keV energy band.

normalization parameters of the apec components correspond to $\frac{10^{-14}}{4\pi d^2} \int n_e \, n_H \, dV$ where d is the distance to the source in cm, whilst n_e and n_H are the electron and hydrogen densities (in cm^{-3}).

Martins et al. (2012) and Martins et al. (2015) analysed the nitrogen and CNO content of HD 108, concluding that the star displays a N enhancement by about a factor of 5 with respect to solar abundances of Asplund et al. (2009), while C and O are depleted by factors of 0.6 and 0.5, respectively. Since lines of hydrogen-like and helium-like ions of C, N, and O are present in the X-ray spectrum below 1 keV, these non-solar abundances could impact the results of the spectral fits. We thus reanalysed the spectra with a model [phabs$_{\rm ISM}$ × (phabs$_1$ × vapec(kT$_1$) + phabs$_2$ × vapec(kT$_2$))] where the vapec plasma models indicate apec models with non-solar abundances. We fixed the C, N, and O abundances, respectively, to 0.6, 5.0, and 0.5 times solar and kept all other elements at a solar abundance. The results of these fits are described in the lower half of Table 4. These modified abundances slightly improve the quality of the fits, but overall do not change the global results significantly.

Our parameters for the *XMM-Newton* observation slightly differ from those reported by Nazé et al. (2004) and Nazé et al. (2014). Several factors could explain these differences: inclusion of the RGS data in our present fit, different model formulation (global or individual circumstellar absorptions, mekal – Kaastra & Mewe 2000 – versus apec – Smith et al. 2001 – plasma models), different versions
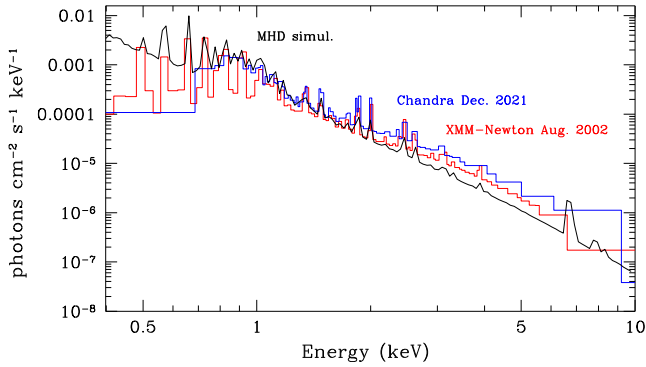
Figure 11. Unfolded X-ray model spectra of HD 108 as adjusted to the *XMM-Newton* August 2002 (rotation phase $\simeq 0.41$) spectra shown in red and the *Chandra* December 2021 (rotation phase $\simeq 0.77$) data displayed in blue. The models were computed with the CNO abundances of Martins et al. (2015). The black line yields the spectral energy distribution predicted by our MHD calculations corresponding to Model II parameters (see the forthcoming Section 5.2).

of the xspec software (and thus of atomic parameters), different abundances (solar abundances taken from Anders & Grevesse 1989 in the previous studies versus abundances from Asplund et al. 2009, or modified according to Martins et al. 2015 here), and evolving knowledge of the calibrations of the *XMM-Newton* instruments. Following some trials, the most important reason appears to be the evolving instrument calibration, with the other effects accounting for flux differences of a few per cent at most.

We also stress that one must be careful when interpreting the parameters in Table 4. First of all, there exists a well-known degeneracy between the column density of the material responsible for the photoelectric absorption and the temperature of the emitting plasma. Especially in the case of low-resolution CCD spectra, a given spectrum can be equally well represented by a low-temperature plasma absorbed by a high column density or a higher temperature plasma seen through a lower column density. This degeneracy most strongly affects the kT_1 component and the associated column density $N_{H, 1}$. It typically affects the results as seen in the *XMM* versus *Chandra* fittings (low N_H and high kT versus high N_H and lower kT). However, since the spectral energy distribution is well fitted, this degeneracy does not alter much the derived X-ray fluxes. Second, there remain some cross-calibration uncertainties between *XMM-Newton* and *Chandra*. These can affect both the plasma parameters and the inferred fluxes. Using observations of the line-rich supernova remnant (SNR) 1E 0102.2-7219 by *Chandra*, *Suzaku*, *Swift* and *XMM-Newton*, Plucinsky et al. (2012) showed that the fluxes of the prominent lines in the 0.5–1.5 keV domain measured by these satellites agree within 10 per cent. At higher energies, Madsen et al. (2021) found differences of ~15 per cent between *Chandra* and *XMM-Newton* in the 4.5–8.0 keV domain for the SNR N 132D. Based on this, we consider that the fluxes derived from our X-ray observations of HD 108 could be affected by cross-calibration uncertainties of 10–15 per cent.

Nevertheless, the *Chandra* observation yields an observed flux in the 0.5–10 keV band that is 28 per cent higher than that recorded in the *XMM-Newton* observation. Hence, the flux very probably increased between the two observations (i.e. between rotation phase $\simeq$ 0.41 and $\simeq$ 0.77), but the increase is rather modest when looking at the full energy band. Fig. 11 illustrates the unfolded spectra of both observations. In general, accounting for the different widths of the energy bins, the overall shapes of the spectra are in good agreement. Yet, the *Chandra* observation yields a somewhat higher flux especially at higher energies. While the *Chandra* flux is 18 per cent higher than the *XMM-Newton* flux at energies between 0.5 and 2.0 keV, the increase amounts to 50 per cent at energies between 2.0 and 10 keV. If we consider the X-ray flux corrected for the interstellar absorption (but not corrected for the circumstellar absorption), then the two observations yield the same flux in the soft (0.5–2.0 keV) band, but a 50 per cent increase is still seen in the hard (2.0–10 keV) domain.

The *GAIA* EDR3 (Gaia Collaboration et al. 2021) lists a parallax of 0.4980 ± 0.0240 mas for HD 108, which according to Bailer-Jones et al. (2021) translates into a distance of (1.91 ± 0.11) kpc. Adopting this distance, the *XMM-Newton* observation yields an X-ray luminosity corrected for interstellar absorption of $L_X = 5.0 \, 10^{32}$ erg s^{-1} in the 0.5–10 keV band, while the *Chandra* observation yields $L_X = 5.5 \, 10^{32}$ erg s^{-1}. Scaling the bolometric luminosity determined by Martins et al. (2012) to the *Gaia* distance, we finally infer $\log L_X/L_{bol} = -6.35$ and $\log L_X/L_{bol} = -6.31$ respectively for the *XMM-Newton* and *Chandra* data. These values clearly place HD 108 among the X-ray fainter Of?p stars, but are still fully compatible with other magnetic O-type stars ($\log L_X/L_{bol}$ value of -6.23 ± 0.07 on average, Nazé et al. 2014).

Comparing the *XMM-Newton* X-ray flux to previous *Einstein* (1979) and *ROSAT* (1991) data, Nazé et al. (2004) noted the absence of strong variations (by more than a factor of two). Our results confirm the relatively low amplitude of the variation of the X-ray flux. We can further compare the behaviour of HD 108 to that of other Of?p stars. For HD 191 612, a ~40 per cent variation of the X-ray fluxes (both the observed and the ISM-corrected values) between high and low state was measured (Nazé et al. 2007). Similar to HD 108, the X-ray spectrum of HD 191 612 is also dominated by the cooler spectral component. CPD $-28°$ 2561 was found to display bright and hard X-ray emission which varies in fluxes by ~55 per cent in phase with the optical variations (Nazé et al. 2015a). No significant hardness variations were found between minima and maxima for this star. Hence, from the data recorded so far, and accounting for the fact that the maximum emission has not yet been reached, the level of variability of HD 108's X-ray emission appears similar to that of other Of?p stars.

The detection of a binary signature in Section 3.4 raises the question whether or not the secondary star or a wind interaction between the Of?p star and the secondary could contribute significantly to the X-ray emission of HD 108. Given the likely mass of the secondary and assuming it to be a non-degenerate star, its intrinsic X-ray emission should be several orders of magnitude lower than the emission of the Of?p star. Such a star would also have a very weak wind, implying that any putative wind interaction would most likely consist in a collision of the Of?p wind with the companion's photosphere. Given the wide orbital separation, such an interaction would only concern a very small part of the Of?p wind. Thus, the associated X-ray emission should be negligible. Finally, if we assume the secondary to be a degenerate object, it would have to be a black hole given the minimum mass we have inferred. Accretion by such an object should lead to a very different spectral energy distribution than the one observed. Hence, we conclude that the companion is unlikely to play a role in the X-ray emission of HD 108. Beside the emission from the hot plasma of the magnetically confined wind, some soft X-ray emission could arise from intrinsic wind instabilities. The latter should typically account for $\log L_X/L_{bol} \simeq -7$, i.e. about 25 per cent of the observed X-ray emission.

Table 5. Adopted parameters of HD 108.

Parameter	Adopted value	Reference	Model I	Model II	Model III
d (kpc)	1.91 ± 0.11	Bailer-Jones et al. (2021)			
$T_{\rm eff}$ (kK)	35 ± 2	Martins et al. (2012)			
$\log \frac{L_{\rm bol}}{L_\odot}$	5.46 ± 0.10	This work			
R_* ($R_\odot$)	14.7 ± 1.2	This work			
$M_{*,\rm evol}$ ($M_\odot$)	38.5 ± 4	This work			
$\log(\dot{M})$ ($M_\odot\,{\rm yr}^{-1}$)	-6.06 ± 0.23	This work			
$v_{\rm esc}$ (km s^{-1})	890 ± 60	This work			
v_∞ (km s^{-1})	2300 ± 300	This work			
$B_{\rm d}$ (G)	≥ 1150	Shultz & Wade (2017)	1150	2000	4000
η_*			27.5	83.1	332.4
R_A (R_*)			2.59	3.32	4.57

5 THE MAGNETOSPHERE OF HD 108

Martins et al. (2010) first reported the spectropolarimetric signature of the magnetic field of HD 108. The longitudinal field strength was found to increase between 2007, 2008, and 2009, as the star was emerging from its minimum state (Martins et al. 2010). These measurements suggested a dipolar magnetic field of at least 0.5 kG, but more likely 1–2 kG. In January 2010, Hubrig, Ilyin & Schöller (2010) detected a magnetic field with a longitudinal strength marginally higher than that found by Martins et al. (2010). Shultz & Wade (2017) presented a new spectropolarimetric observation of HD 108 taken in September 2015 that yielded $<B_z> = -325 \pm 45$ G, about three times the value measured by Martins et al. (2010). This led to a revised minimum value of the dipolar field strength of 1150 G (Shultz & Wade 2017).

For a dipolar magnetic field tilted by an obliquity angle β with respect to the stellar rotation axis, the strength of the longitudinal field should vary with time as a simple sine wave (Preston 1967; Donati et al. 2002):

$$< B_z > = B_d \, \frac{15 + u}{20\,(3 - u)} \, (\cos\beta\,\cos i + \sin\beta\,\sin i\,\cos(2\pi\,\phi)) \quad (2)$$

where i is the inclination of the rotation axis with respect to the line of sight, u is the continuum linear limb darkening coefficient, and $\phi = \frac{(t-t_0)}{P_{\rm rot}}$ is the phase of the stellar rotation with $\phi = 0$ at t_0 when the magnetic axis is closest to our line of sight. For stars with effective temperatures and gravities close to those of HD 108, Claret (2019) quotes values of u between 0.22 and 0.35. However, this range of values translates only into a small change of $<B_z>$ by about 5 per cent. Adopting $u = 0.3$, and accounting for the fact that B_d has a negative value, one finds that the minimum value of the longitudinal field amounts to

$$< B_{z,\rm min} > = 0.283 \, B_d \, \cos(\beta - i)$$

while its maximum value is given by

$$< B_{z,\rm max} > = 0.283 \, B_d \, \cos(\beta + i)$$

In principle, the values of B_d, i and β can be constrained by adjusting equation (2) to the values of $<B_z>$ determined at different rotational phases. Yet, in the case of HD 108, the currently existing spectropolarimetric data do not provide a sufficient sampling of the 54 yrs cycle to fit all parameters independently. Moreover, the uncertainties on the existing measurements allow for a rather wide range of B_d values, even when we fix the i and β angles to the values we infer from the EW(Hα) light curve (see Section 5.1). Nevertheless, even though we cannot infer a precise B_d value at this stage, the existing data suggest a value of B_d which is likely

somewhere between 2000 G and 4000 G. We thus tested models with B_d values of 1150 G (Model I), 2000 G (Model II), and 4000 G (Model III, see Table 5) in our calculations hereafter.

Fundamental stellar and wind parameters of HD 108 were determined by Martins et al. (2012) assuming a distance of 2.51 kpc. Using instead the revised distance determined by Bailer-Jones et al. (2021), we have scaled these parameters to infer $R_* = (14.7 \pm 1.2)\,R_\odot$, $\log \frac{L_{\rm bol}}{L_\odot} = 5.46 \pm 0.1$, and $M_{*,\rm evol} = 38.5 \pm 4\,M_\odot$.

Observationally-determined values of the mass-loss rate (e.g. Martins et al. 2010; Marcolino et al. 2012) were derived by means of model atmosphere codes that assume a spherically symmetric and homogeneous wind and hence do not account for the actual wind geometry and the action of the magnetic field on the wind. To evaluate the impact of the magnetic field on the outflow, one must instead use the value of $\dot{M}_{B=0}$ that would be observed in the absence of a magnetic field (ud-Doula & Owocki 2002). Therefore, Shultz & Wade (2017) estimated $\dot{M}_{B=0}$ via the formalism of Vink, de Koter & Lamers (2001) that predicts a mass-loss rate of $2.8\,10^{-6}\,M_\odot\,{\rm yr}^{-1}$, about 1 dex higher than the value inferred from spectroscopic analyses of the ultraviolet spectrum (Martins et al. 2010; Marcolino et al. 2012). Using instead the luminosity and stellar mass estimates that stem from the revised distance determination, the Vink et al. (2001) recipe leads to a lower value of $\dot{M}_{B=0} = 0.9\,10^{-6}\,M_\odot\,{\rm yr}^{-1}$ ($\log \dot{M}_{B=0} = -6.06 \pm 0.23$).

Similar remarks apply to the asymptotic wind velocity v_∞. In the computation of the wind confinement parameter $\eta_* = \frac{B_d^2\,R_*^2}{4\,\dot{M}_{B=0}\,v_\infty}$ (e.g. ud-Doula & Owocki 2022, and references therein) and in the MHD simulations, one needs the value of v_∞ that would be observed in the absence of a magnetic field. Typical values of the $v_\infty/v_{\rm esc}$ ratio are expected to be around 2.6, which would lead to $v_\infty \simeq (2300 \pm 150)\,{\rm km\,s}^{-1}$. The resulting model parameters are summarized in Table 5.

5.1 Fitting the EW variations with an analytic dynamical magnetosphere-type model

In the oblique magnetic rotator model, the axis of the dipolar magnetic field is inclined by an obliquity angle β with respect to the stellar rotational axis. The rotation axis itself is seen under an inclination i by the external observer. The optical emission lines are strongest when the magnetically confined wind is seen as much as possible face-on, i.e. when the angle between the direction of the dipolar magnetic field and the line of sight is minimum and amounts to $\beta - i$. Conversely, the emission lines are weakest when the magnetosphere is seen near edge-on, i.e. when the angle between the magnetic axis and the line of sight is equal to $\beta + i$.
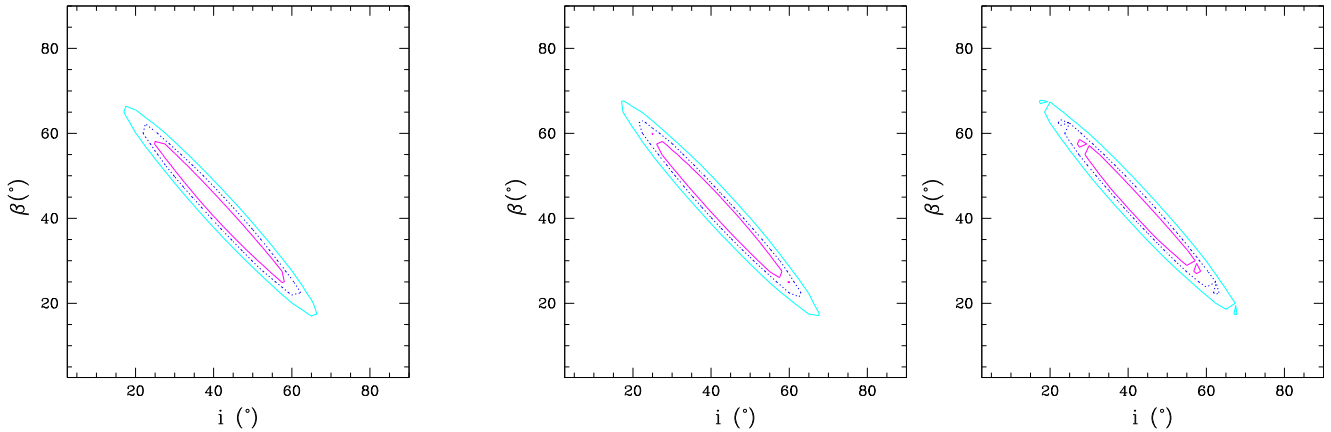
Figure 12. χ^2 contours of the ADM models for $\delta/R_* = 0.1$. The different contours correspond to values of the reduced χ^2 of $\chi^2_{min} + 2.30$ (magenta solid line), $\chi^2_{min} + 4.61$ (blue dotted line), and $\chi^2_{min} + 9.21$ (cyan dashed line). The left panel assumes parameters of Model I ($\chi^2_{min} = 1.53$), the middle panel stands for Model II ($\chi^2_{min} = 1.75$), while the right panel corresponds to Model III ($\chi^2_{min} = 1.57$).

Owocki et al. (2016) designed an analytic dynamical magnetosphere (ADM) model that provides analytical relations to express the temperature, density, and flow velocities of the different ingredients of the stellar wind and of a dynamical magnetosphere. This model has been used successfully by Munoz et al. (2020) to analyse the optical photometric light curves of several Galactic and Magellanic Cloud Of?p stars as the result of occultations of the stellar photosphere by regions of different densities. In their description, Owocki et al. (2016) distinguish three components of the magnetosphere:

(i) the wind upflow, driven by radiation pressure at the stellar surface and channeled along the magnetic field lines,

(ii) the hot (several MK) post-shock gas, which is produced when the wind upflowing along a closed magnetic loop encounters a hydrodynamic shock as it approaches the magnetic equator, and

(iii) the cooled downflow, made of post-shock gas that has undergone radiative cooling and falls back to the star.

In MHD simulations, these flows are intermingled, forming complex, variable, three-dimensional (3D) structures (e.g. ud-Doula et al. 2013). The ADM model instead considers a time-averaged structure, where the stochastic variations are smoothed out, thereby allowing to infer analytic expressions for the velocities and densities of all three components (Owocki et al. 2016). As far as the optical line emission is concerned, it is mostly the cooled downflow that matters.

To compare the observed line strengths with model calculations, we must correct the observed values for the strength of the underlying photospheric absorption line. Martins et al. (2012) determined an effective temperature of $T_{eff} = (35 \pm 2)$ kK and a log g of 3.50 ± 0.10. Using a TLUSTY synthetic spectrum (Lanz & Hubeny 2003) with these parameters, we estimate the EW of the photospheric Hα absorption to be 2.6 Å. Hence, the 2022–2023 spectra (with the strongest Hα emission observed so far) correspond to a net EW of the Hα emission of -12.6 Å.

To formulate constraints on i and β, we implemented the ADM formalism for EW(Hα) following the prescription for the cooled downflow [equations (22) and (25) of Owocki et al. 2016]. We assumed that the radiative transfer can be treated by means of the Sobolev escape probability approximation (e.g. Rybicki & Hummer 1978). The optical depth in the Hα line measured from a position $\vec{r}$

along the direction $\vec{n}$ towards the observer hence becomes

$$\tau(\vec{r}, \vec{n}) = \frac{6.6\ 10^{20}\ T^{-1.5}}{|Q|} \frac{1 + y_{He}\ I_{He}}{(1 + 4\ y_{He})^2} \rho^2$$
$$\times \left[b_2 \exp\left(\frac{3.3944\ 10^4}{T}\right) - b_3 \exp\left(\frac{1.753\ 10^4}{T}\right) \right] \quad (3)$$

[see equation (1) of Petrenz & Puls 1996]. Here, T and ρ are the gas temperature and gas density at the position $\vec{r}$, y_{He} and I_{He} are the number abundance of helium and the number of free electrons provided per helium atom, and b_2 and b_3 are the non-local thermodynamic equilibrium (NLTE) departure coefficients of the $n = 2$ and $n = 3$ energy levels of the hydrogen atom computed following the parametrization of Puls et al. (1996). The quantity Q stands for the projection of the gradient of the line-of-sight component of the gas velocity onto the line of sight $\vec{n}$ (Rybicki & Hummer 1978) and is given by

$$Q = \vec{n} \cdot \vec{\nabla}(\vec{v} \cdot \vec{n}) \quad (4)$$

Using the stellar and wind parameters of Models I, II, and III from Table 5, we computed grids of ADM models for i and β between 2.5° and 90° with steps of 2.5°. For each pair of i and β, we computed a full synthetic EW(Hα) curve as a function of rotational phase. A rescaled version of this curve, to match the mean level of the observed EW(Hα), was then compared to the observed data points. The rescaling is needed to account for the effects of clumping. Indeed, the fact that the emissivity scales as ρ^2 implies that the clumpiness of the downflow affects the overall emission strength. Such a clumping is seen in the MHD simulations (e.g. ud-Doula et al. 2013) and thus probably exists also in the genuine Of?p magnetosphere, but it is not included in the ADM calculations. The comparison between the rescaled synthetic light curve and the observed data then allowed us to compute χ^2 maps that unveil those values of i and β that yield the best formal match to the observations. Owocki et al. (2016) introduced a parameter δ/R_* that expresses the smoothing of the density near the magnetic equator in the ADM. In our calculations, we considered three different values of this parameter (0.0, 0.1, and 0.3). Fig. 12 illustrates the χ^2 contour plot in the (i, β) parameter space for $\delta/R_* = 0.1$ which, among the three values tested here, yields the best matches between the synthetic curve and our data.

Munoz et al. (2020) showed that photometric light curves computed with the ADM model were subject to a degeneracy between i and β. A very similar degeneracy applies to our analysis. Indeed, our
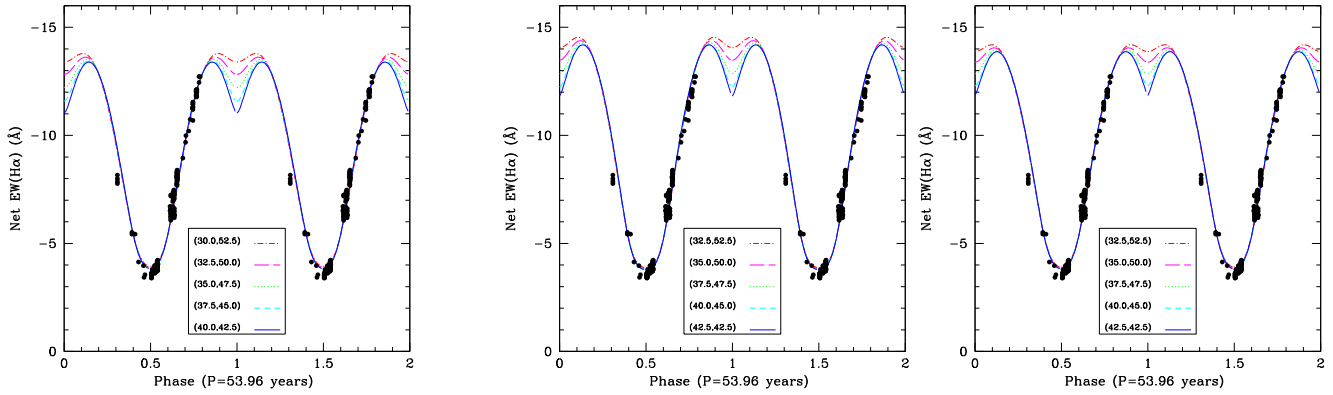
Figure 13. Fit to the net (absorption-corrected) EW(Hα) light curve of HD 108 with ADM models (from left to right Models I, II, and III parameters are used). Different pairs of (i, β) that yield comparable fits to the part of the curve that is sampled with the existing data are illustrated by different colours.

existing EW(Hα) light curve samples HD 108's minimum emission state well, but does not yet cover the phases of maximum emission state. Thus, we expect the value $i + \beta$ to be better constrained than the value of $i - \beta$. Our contour plots indeed unveil the ensuing degeneracy between i and β. For Model I, the best formal fits are obtained for $i = 40.0°$ and $\beta = 42.5°$ but (i, β) pairs with $i + \beta = 82.5°$ and $i \in [27.5°, 55°]$ yield essentially the same fitting quality (see Fig. 13). For Models II and III, the same degeneracy is observed with a slightly higher value of $i + \beta = 85°$, a formally best fit at $i = \beta = 42.5°$, and an acceptable range of inclinations of $i \in [30°, 55°]$. Therefore, the fits of the current EW(Hα) light curve are relatively independent of the assumed value of B_d. As expected in Section 3.2, our best-fit (i, β) pairs differ from those of HD 191 612 for which Owocki et al. (2016) rather inferred $(i, \beta) = (23°, 73°)$ or $(73°, 23°)$.

5.2 Magnetohydrodynamic simulations

We performed a fully self-consistent MHD simulation of HD 108 using the stellar parameters listed in Table 5. For this purpose, we used the publicly available MHD code Zeus-3D adapted to our own needs.

The magnetospheres of massive stars are divided into two broad categories depending on the comparison between the Keplerian corotation radius R_K and the Alfvén radius R_A (Petit et al. 2013). Situations where $R_K < R_A$, corresponding to rapid rotators, are called centrifugal magnetospheres. In those stars, the trapped wind material accumulates in a stable long-lived rigidly rotating disk-like structure. For slow rotators, one has instead $R_K > R_A$. Material from these so-called dynamical magnetospheres falls back onto the star. Owing to its very slow rotation, HD 108 clearly belongs to the class of stars with dynamical magnetospheres.

The extremely slow rotation of HD 108 simplifies the MHD simulations of the star's magnetosphere. Indeed, in such a case, rotation has no significant dynamical effects on the magnetospheric structure. As such, it can thus be modeled with two dimensional (2D) simukations assuming a field aligned with the rotation axis (Sundqvist et al. 2012). We follow the basic methods and formalism presented for 2D simulations by ud-Doula & Owocki (2002), and extended by Gagné et al. (2005) to include a full energy equation with optically thin radiative cooling (MacDonald & Bailey 1981). Following ud-Doula & Owocki (2002), we use radiative driving by line-scattering based on the standard CAK (Castor, Abbott & Klein

1975) formalism, corrected for the finite cone angle of the star, using a spherical expansion approximation for the local flow gradients (Friend & Abbott 1986; Pauldrach, Puls & Kudritzki 1986).

The computational grid and boundary conditions are adopted from ud-Doula & Owocki (2002) and ud-Doula, Owocki & Townsend (2008) to include the non-zero azimuthal velocity at the lower boundary arising from rotation. We use 300 radial grid points logarithmically stretched from stellar surface to 20 stellar radii with a 2 per cent increase in length, i.e. the ratio between two subsequent zones is 1.02. For the mesh in co-latitude, again following ud-Doula & Owocki (2002), we use 100 grid points with a higher number of points around the magnetic equator to capture the compressed disk structure more efficiently. We ran our model for 6 Ms which is long enough to be free from transients resulting from any initial condition.

A snapshot of the structure of the magnetosphere (taken at 6 Ms) corresponding to Model II is shown in Fig. 14. The X-ray emission of each grid cell is computed assuming an optically thin plasma and taking $n_e = n_H$. The synthesized X-ray luminosity integrated between 0.1 and 10 keV of this simulation is $2.48 \, 10^{33} \, \mathrm{erg \, s^{-1}}$, while it amounts to $7.3 \, 10^{32} \, \mathrm{erg \, s^{-1}}$ between 0.5 and 10.0 keV. These synthetic luminosities assume no stellar occultation or absorption by the stellar wind and thus represent an upper limit to the observable luminosity. Stellar wind absorption would mostly affect the softer part of the X-ray spectrum (below 2 keV). However, significant absorption by the circumstellar material has been securely detected only in the extreme case of NGC 1624-2 (Petit et al. 2015). On the contrary, given that the X-ray emission arises at a distance of about $3.5 \, R_*$ (Fig. 14), occultation effects will only play a role at rotational phases close to the minimum state. With these caveats in mind, the 0.5–10 keV luminosity predicted by the model is in very good agreement with the observationally-determined values (see Section 4). Fig. 11 further shows that the spectral energy distribution predicted by the Model II MHD calculations nicely matches the observed one.

Very similar values of the X-ray luminosities are obtained for Model I ($2.52 \, 10^{33}$ and $7.7 \, 10^{32} \, \mathrm{erg \, s^{-1}}$), while Model III yields lower values ($9.8 \, 10^{32}$ and $2.2 \, 10^{32} \, \mathrm{erg \, s^{-1}}$). At first sight, it is surprising to see Model III produce less X-ray emission than the two other models with lower magnetic field strengths as this is contrary to the predictions of the X-ray analytic dynamical magnetosphere (XADM) paradigm (ud-Doula et al. 2014). However, HD 108's wind properties result in a wind cooling parameter χ_∞ at the border between the adiabatic and radiative regimes. Any small deviation in the wind
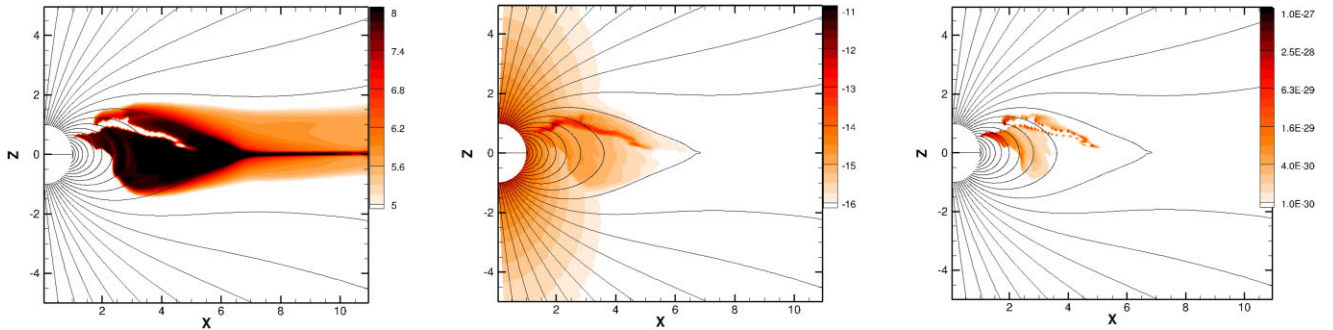
Figure 14. Snapshot of the 2D MHD simulation of the magnetically confined wind of HD 108 (Model II) at 6 Ms after the onset of the simulation. The z axis indicates the direction of the magnetic dipole axis. From left to right, the panels illustrate the logarithm of the plasma temperature (in K), the logarithm of the density (in g cm^{-3}), and the emission measure of the plasma (in g^2 cm^{-6}) with $T \geq T_{\mathrm{thresh}} = 1.5$ MK (equivalent to $kT_{\mathrm{threshold}} = 0.13$ keV). The emission measure is defined as $\rho^2 \exp(-T/T_{\mathrm{thresh}})$ (ud-Doula et al. 2014).
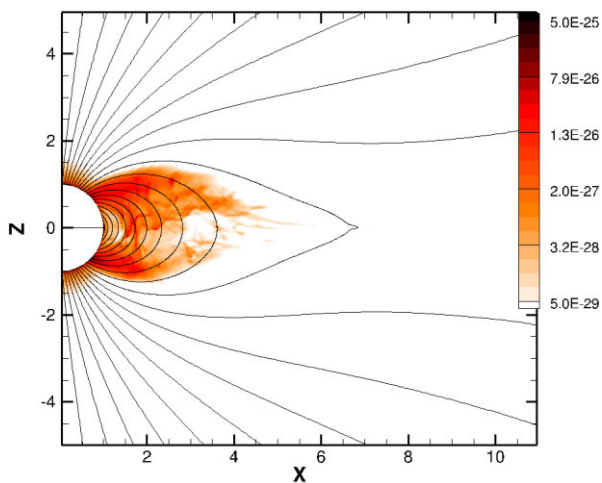
Figure 15. Time-averaged ρ^2 distribution as inferred from the 2D MHD simulation of Model II.

parameters can thus lead to significant changes in the ensuing X-ray emission. In particular, the much higher magnetic confinement parameter in Model III leads to much larger closed loops wherein wind speed can substantially exceed the presumed v_∞ of the non-magnetic wind, thus making cooling much less efficient as the cooling parameter is very sensitive to speed ($\chi_\infty \propto v^4$). This in turn enhances the shock retreat effects wherein less efficient cooling pushes the shock back along the loops towards the star, hence to lower pre-shock wind speeds. As a result, the X-ray emission becomes softer and weaker. Further studies will be required to investigate this issue in more details.

The emission measure plot (right panel of Fig. 14) indicates that the bulk of the X-ray emission in Model II is generated between about 1.5 and 3.5 R_* (i.e. out to the Alfvén radius). Though the simulation also predicts hot material with a kT above 0.13 keV beyond this region (left panel of Fig. 14), this plasma is too tenuous to contribute significantly to the overall X-ray emission as revealed by comparing the left and right panels of Fig. 14.

The variable optical emission lines are expected to arise from the radiatively cooled magnetospheric material that falls back to the stellar surface (Sundqvist et al. 2012; Owocki et al. 2016). Since the Hα line emission is formed via the recombination process, the best indicator of the line forming region is ρ^2. Fig. 15 indicates that most of the optical line emission is expected

to arise from material located between the stellar surface and about 3.5 R_*, i.e. from within the Alfvén radius ($R_A = 3.3\,R_*$ for Model II).

6 DISCUSSION AND CONCLUSIONS

In this study, we analysed optical and X-ray spectra of the Of?p star HD 108 to constrain the properties of this star and its magnetosphere. Beside the 54 ± 3 yrs cycle that modulates the strength of most emission lines, our data unveil an 8.5 yr periodic variation of the radial velocities with a peak-to-peak amplitude of 10–11 km s^{-1}. This is strong evidence for binarity with an unseen companion of at least 4 M$_\odot$. Alike two other Of?p stars, HD 108 thus also is a binary system, although the binary properties (orbital period, eccentricity, etc.) differ strongly among these three objects.

The variable emission lines in the optical spectrum of HD 108 have now recovered from the minimum emission state that was reached in the years 2007–2008. While our spectroscopic monitoring of HD 108 with modern instrumentation does not yet cover the full 54 yr cycle, our fitting of the EW(Hα) light curve with an ADM model yields constraints on the inclination angle of the rotation axis (i) and the obliquity of the magnetic axis (β). We find that pairs of (i, β) that satisfy $i + \beta \simeq 85°$ with $i \in [30°, 55°]$ yield results of similar quality. This implies that near minimum state, the magnetosphere was seen under an angle of 85°, i.e. almost edge-on. The detection of inverse P-Cygni-type profiles in the Si III $\lambda\lambda$ 4552, 4568, 4575 lines around the 2007–2008 minimum state (see the left panel of Fig. 2) then clearly indicates that these lines arise in material that was observed to flow back to the stellar surface. This line morphology is fully consistent with our configuration of the magnetically confined wind: around minimum state, the magnetosphere is seen nearly edge-on and the backfalling material where the Si III emissions arise is seen projected against the stellar disk.

TESS photometry of HD 108 unveiled a strong red noise variability which likely reflects the same phenomenon as the macroturbulence that broadens the spectral lines of this very slow rotator. Beside this red noise component, the *TESS* data also display a transient cyclic modulation on a timescale of about 6 d. We found similar, though not identical, time-scales in the short-term variations of the Hα emission. This suggests a possible link between the transient photometric cycle and the spectroscopic variability. Although we cannot rule out a purely photospheric origin, this variability could also arise from episodes of enhanced downflow of magnetospheric material. Indeed, Barannikov (2007) reported on a slow photometric
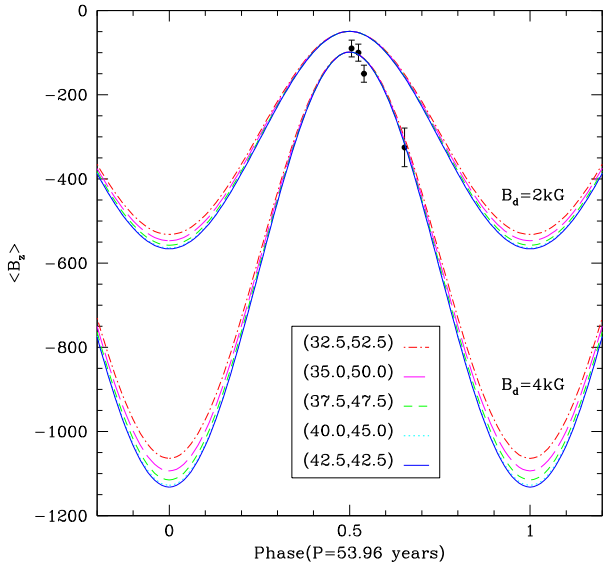
Figure 16. Predicted values of $<B_z>$ computed with equation (2) for the (i, β) pairs found in Section 5.1 (see Fig. 13). Two different values of B_d have been tested. The points with their error bars stand for the data from Martins et al. (2010) and Shultz & Wade (2017).

fading of HD 108 as the star was going to the minimum emission state. This suggests that reflection of photospheric light by cool material in the magnetosphere contributes to the optical brightness of this star. The same cool magnetospheric material is responsible for the Hα emission. The existence of modulations on time-scales of ~ 4–8 d in photometry and line emission strength could thus reflect a roughly cyclic behaviour of the magnetosphere, where material first piles up locally before it cools and falls back to the star.

The best-fit ADM models predict that the emission strength should further increase by about 1.4 Å in the coming decade. Spectroscopic monitoring of the star in the coming decade will show whether the light curve near phase 0.5 is flat or presents a secondary dip, thus leading to even more stringent constraints on i and β. Meanwhile, our results indicate that the dipolar magnetic field strength B_d of HD 108 is probably significantly stronger than the value previously estimated by Martins et al. (2010) or Shultz & Wade (2017). Indeed, in an oblique magnetic rotator, the emission lines are strongest when the magnetically confined wind is seen near face-on, i.e. when the angle between the direction of the dipolar magnetic field and the line of sight is minimum. Fig. 16 illustrates the value of $<B_Z>$ computed with equation (2) (Donati et al. 2002) for the different pairs of i and β allowed by our ADM models and assuming values of B_d of -2000 or -4000 G. While the existing spectropolarimetric determinations of $<B_z>$ are not sufficient to achieve a precise evaluation of B_d, the figure clearly shows that they are in much better agreement with values of B_d of -4000 G than with values of -2000 G or lower. Forthcoming spectropolarimetric observations of HD 108 should thus indicate significantly larger values of $<B_z>$, hence allowing to further constrain the value of HD 108's dipolar magnetic field strength.

The *GAIA* distance determination of HD 108 led to a revision of the star's mass-loss rate. This could have important implications on the spin-down time. Indeed, the value of the magnetic field originally determined by Martins et al. (2010) and the low value of $\dot{M}$ inferred by Marcolino et al. (2012) implied an upper limit on the spin-down time more than twice longer than the estimated age of HD 108 (Petit et al. 2013). Shultz & Wade (2017) obtained a higher value

of $<B_z>$ which solved this issue, provided the stellar wind mass-loss rate was taken to be $2.8\,10^{-6}\,M_\odot\,yr^{-1}$. In this paper, we have shown that scaling the stellar parameters to the *GAIA* distance yields a lower $\dot{M}_{B=0}$ of $0.9\,10^{-6}\,M_\odot\,yr^{-1}$. The spin-down time-scale τ_J depends on the stellar mass-loss time-scale ($M_*/\dot{M}_{B=0}$) and the wind confinement parameter η_* (ud-Doula et al. 2008; ud-Doula & Owocki 2022). Using equation (8) of ud-Doula & Owocki (2022) with the parameters of Table 5, we infer τ_J values of $9.9\,10^5$, $6.0\,10^5$, and $3.2\,10^5$ yr, respectively for Models I, II, and III. As shown above, Models II and especially III are in better agreement with the existing $<B_z>$ measurements. We thus conclude that τ_J is most probably in the range $3.2\,10^5$ to $6.0\,10^5$ yr. The maximum spin-down age, assuming the star was at critical rotation initially, is then given by $t_{s,max} = -\tau_J \ln W$ where $W = V_{rot}/\sqrt{G\,M_*/R_*}$ is the present-day critical rotation fraction. Again using the parameters of Table 5, we obtain $W \simeq 5.3\,10^{-5}$ and thus $t_{s,\,max}$ between 3.1 and 5.9 Myr, respectively, for $B_d = -4000$ G and $B_d = -2000$ G. With the revised distance determination, HD 108 would have an evolutionary age of about 3.5 Myr (Martins et al. 2012). We thus conclude that the spin-down age is consistent with the evolutionary age provided that the dipole field strength is indeed near 4 kG.

Our observations of HD 108 indicate that our sightline is now nearly aligned with the magnetic axis, allowing us to gain precious insight into the properties of its magnetosphere. Continuing the monitoring of this star in optical spectroscopy, spectropolarimetry and X-ray spectroscopy over at least another decade will allow to finally lift the remaining ambiguities.

DATA AVAILABILITY

The *TESS* data underlying this article are available from the MAST archives, whereas the OHP and TIGRE spectra can be made available upon reasonable request. *Chandra* and *XMM-Newton* data are available from their respective archives.

REFERENCES

Aerts C., Rogers T. M., 2015, ApJ, 806, L33
Aerts C. et al., 2017, A&A, 602, A32
Anders E., Grevesse N., 1989, Geochimica et Cosmochimica Acta, 53, 197
Andrillat Y., Fehrenbach C., Swings P., Vreux J.-M., 1973, A&A, 29, 171
Aslanov A. A., Barannikov A. A., 1989, Soviet Astron. Lett., 15, 316
Asplund M., Grevesse N., Sauval A. J., Scott P., 2009, ARA&A, 47, 481
Babel J., Montmerle T., 1997, ApJ, 485, L29
Bailer-Jones C. A. L., Rybizki J., Fouesneau M., Demleitner M., Andrae R., 2021, AJ, 161, 147
Barannikov A. A., 1999, Astron. Lett., 25, 169
Barannikov A. A., 2007, IBVS, 5756, 1
Blomme R. et al., 2011, A&A, 533, A4
Bowman D. M. et al., 2019, Nat. Astron., 3, 760
Bowman D. M., Burssens S., Simón-Díaz S., Edelmann P. V. F., Rogers T. M., Horst L., Röpke F. K., Aerts C., 2020, A&A, 640, A36
Brucato R. J., 1971, MNRAS, 153, 435
Cantiello M. et al., 2009, A&A, 499, 279
Cantiello M., Lecoanet D., Jermyn A. S., Grassitelli L., 2021, ApJ, 915, 112
Castor J. I., Abbott D. C., Klein R. I., 1975, ApJ, 195, 157
Claret A., 2019, Res. Notes Am. Astron. Soc., 3, 17
Diplas A., Savage B. D., 1994, ApJS, 93, 211
Donati J.-F., Babel J., Harries T. J., Howarth I. D., Petit P., Semel M., 2002, MNRAS, 333, 55
Donati J.-F., Howarth I. D., Bouret J.-C., Petit P., Catala C., Landstreet J., 2006, MNRAS, 365, L6
Friend D. B., Abbott D. C., 1986, ApJ, 311, 701
Fullerton A. W., Gies D. R., Bolton C. T., 1996, ApJS, 103, 475
Gagné M. et al., 2005, ApJ, 628, 986
Gaia Collaboration, 2021, A&A, 649, A1
Gillet D. et al., 1994, A&AS, 108, 181
González J. F., Levato H., 2006, A&A, 448, 283
González-Perez J. N., Mittag M., Schmitt J. H. M. M., Schröder K.-P., Jack D., Rauw G., Nazé Y., 2022, Front. Astron. Space Sci., 9, 912546
Gosset E., Royer P., Rauw G., Manfroid J., Vreux J.-M., 2001, MNRAS, 327, 435
Grassitelli L., Fossati L., Simón-Díaz S., Langer N., Castro N., Sanyal D., 2015, ApJ, 808, L31
Heck A., Manfroid J., Mersch G., 1985, A&AS, 59, 63
Hinkle K., Wallace L., Valenti J., Harmer D., 2000, in Visible and Near Infrared Atlas of the Arcturus Spectrum 3727-9300 Å. Astron. Soc. Pac., San Francisco
Howarth I. D. et al., 2007, MNRAS, 381, 433
Hubrig S., Ilyin I., Schöller M., 2010, AN, 331, 781
Hutchings J. B., 1975, ApJ, 200, 122
Jansen F. et al., 2001, A&A, 365, L1
Jenkins J. M. et al., 2016, Proc. SPIE, 9913, 99133E
Kaastra J. S., Mewe R., 2000, in Bautista M. A., Kallman T. R., Pradhan A. K., eds, Atomic Data Needs for X-ray Astronomy, NASA CP-2000-209968. p. 161
Kaufer A., 1998, in Arribas S., Mediavilla E., Watson F., eds, ASP Conf. Ser. Vol. 152, Fiber Optics in Astronomy. Astron. Soc. Pac., San Francisco, p. 337
Lanz T., Hubeny I., 2003, ApJS, 146, 417
Lecoanet D. et al., 2019, ApJ, 886, L15
MacDonald J., Bailey M. E., 1981, MNRAS, 197, 995
MacDonald J., Petit V., 2019, MNRAS, 487, 3904
Madsen K. K. et al., 2021, preprint (arXiv:2111.01613)
Mahy L. et al., 2022, A&A, 664, A159
Mannino G., Humblet J., 1955, Annales d'Astrophysique, 18, 237
Marcolino W. L. F. et al., 2012, MNRAS, 422, 2314
Martins F. et al., 2010, MNRAS, 407, 1423
Martins F., Escolano C., Wade G. A., Donati J.-F., Bouret J.-C., 2012, A&A, 538, A29
Martins F. et al., 2015, A&A, 575, A34
Merrill P. W., Humason M. L., Burwell C. G., 1925, ApJ, 61, 389

Mittag M., Hempelmann A., González-Pérez J. N., Schmitt J. H. M. M., Hall J. C., 2011, in Johns-Krull C. M., Browning M. K., West A. A., eds, ASP Conf. Ser. Vol. 448, 16th Cambridge Workshop on Cool Stars, Stellar Systems and the Sun,. Astron. Soc. Pac., San Fransisco, p. 1187
Munoz M. S., Wade G. A., Nazé Y., Puls J., Bagnulo S., Szymański M. K., 2020, MNRAS, 492, 1199
Nazé Y., Vreux J.-M., Rauw G., 2001, A&A, 372, 195
Nazé Y., Rauw G., Vreux J.-M., De Becker M., 2004, A&A, 417, 667
Nazé Y., Barbieri C., Segafredo A., Rauw G., De Becker M., 2006, IBVS, 5693, 1
Nazé Y., Rauw G., Pollock A. M. T., Walborn N. R., Howarth I. D., 2007, MNRAS, 375, 145
Nazé Y., Walborn N. R., Rauw G., Martins F., Pollock A. M. T., Bond H. E., 2008a, AJ, 135, 1946
Nazé Y., Walborn N. R., Martins F., 2008b, Rev. Mex. Astr. Astrof., 44, 331
Nazé Y., ud-Doula A., Spano M., Rauw G., De Becker M., Walborn N. R., 2010, A&A, 520, A59
Nazé Y., Petit V., Rinbrand M., Cohen D., Owocki S., ud-Doula A., Wade G. A., 2014, ApJS, 215, 10
Nazé Y., Sundqvist J. O., Fullerton A. W., ud-Doula A., Wade G. A., Rauw G., Walborn N. R., 2015, MNRAS, 452, 2641
Nazé Y., Neiner C., Grunhut J., Bagnulo S., Alecian E., Rauw G., Wade G.A., et al., 2017, MNRAS, 467, 501
Nazé Y., Rauw G., Pigulski A., 2020, MNRAS, 498, 3171
Nazé Y., Rauw G., Gosset E., 2021, MNRAS, 502, 5038
Owocki S. P., ud-Doula A., Sundqvist J. O., Petit V., Cohen D. H., Townsend R. H. D., 2016, MNRAS, 462, 3830
Pauldrach A., Puls J., Kudritzki R.-P., 1986, A&A, 164, 86
Petit V. et al., 2013, MNRAS, 429, 398
Petit V. et al., 2015, MNRAS, 453, 3288
Petrenz P., Puls J., 1996, A&A, 312, 195
Plucinsky P. P. et al., 2012, Proc. SPIE, 8443, 844312
Preston G. W., 1967, ApJ, 150, 547
Puls J. et al., 1996, A&A, 305, 171
Ramiaramanantsoa T. et al., 2018, MNRAS, 473, 5532
Rauw G., Nazé Y., 2021, MNRAS, 500, 2096
Ricker G. R. et al., 2015, JATIS, 1, 014003
Rogers T. M., Lin D. N. C., McElwaine J. N., Lau H. B. B., 2013, ApJ, 772, 21
Rybicki G. B., Hummer D. G., 1978, ApJ, 219, 654
Sana H., Gosset E., Rauw G., 2006, MNRAS, 371, 67
Schmitt J. H. M. M., Schröder K.-P., Rauw G., Hempelmann A., Mittag M., González-Perez J. N., Czesla S., 2014, AN, 335, 787
Shore S. N., Brown D. N., 1990, ApJ, 365, 665
Shultz M., Wade G. A., 2017, MNRAS, 468, 3985
Smith R. K., Brickhouse N. S., Liedahl D. A., Raymond J. C., 2001, ApJ, 556, L91
Stahl O. et al., 1996, A&A, 312, 539
Stanishev V., Kraicheva Z., Boffin H. M. J., Genkov V., 2002, A&A, 394, 625
Sundqvist J. O., ud-Doula A., Owocki S. P., Townsend R. H. D., Howarth I. D., Wade G. A., 2012, MNRAS, 423, L21
Sundqvist J. O., Petit V., Owocki S. P., Wade G. A., Puls J., 2013, MNRAS, 433, 2497
Trigueros Páez E., Barbá R., Negueruela I., Maíz Apellániz J., Simón-Díaz S., Holgado G., 2021, A&A, 655, A4
ud-Doula A., Nazé Y., 2016, Adv. Space Res., 58, 680
ud-Doula A., Owocki S. P., 2002, ApJ, 576, 413
ud-Doula A., Owocki S. P., 2022, preprint (arXiv:2209.08540)
ud-Doula A., Owocki S. P., Townsend R. H. D., 2008, MNRAS, 385, 97
ud-Doula A., Owocki S. P., Townsend R. H. D., 2009, MNRAS, 392, 1022
ud-Doula A., Sundqvist J. O., Owocki S. P., Petit V., Townsend R. H. D., 2013, MNRAS, 428, 2723
ud-Doula A., Owocki S. P., Townsend R. H. D., Petit V., Cohen D., 2014, MNRAS, 441, 3600
Underhill A. B., 1994, ApJ, 420, 869
Verschueren W., David M., 1999, A&AS, 136, 591
Vink J. S., de Koter A., Lamers H. J. G. L. M., 2001, A&A, 369, 574

Vreux J.-M., Conti P. S., 1979, ApJ, 228, 220
Wade G. A. et al., 2012a, MNRAS, 419, 2459
Wade G. A. et al., 2012b, MNRAS, 425, 1278
Wade G. A. et al., 2015, MNRAS, 447, 2551
Wade G. A. et al., 2019, MNRAS, 483, 2581
Walborn N. R., 1972, AJ, 77, 312
Walborn N. R., 1973, AJ, 78, 1067
Walborn N. R. et al., 2004, ApJ, 617, L61
Walborn N. R., Sota A., Maíz Apellániz J., Alfaro E. J., Morrell N. I., Barbá
    R. H., Arias J. I., Gamen R. C., 2010, ApJ, 711, L143

Weisskopf M. C., Tananbaum H. D., Van Speybroeck L. P., O'Dell S. L.,
    2000, in Truemper J. E., Aschenbach B., eds, Proc. SPIE Conf. Ser. Vol.
    4012, X-Ray Optics, Instruments, and Missions III. SPIE, Bellingham, p.
    2

APPENDIX A: TABLE OF OBSERVATIONS

Table A1 below provides the list of the optical spectra of HD 108 used in this study along with the measured RVs and EWs. The spectra are ordered by date.

Table A1. Journal of our optical spectroscopic observations.

HJD−2400000	Obs.	RVs (km s^{-1})								EWs (Å)						
		He II λ4200	He II λ4542	He II λ4686	N III	O III λ5592	C III λ5696	He II λ4200	Hγ	He I λ4471	Hβ	C III λ5696	He I λ5876	Hα	He I λ6678
46627.5820	OHP	−70.1						0.55							
46628.5480	OHP	−59.5						0.55							
47007.5360	OHP	−77.2						0.51	0.18						
47007.5440	OHP	−78.9						0.51	0.15						
47007.5490	OHP	−82.1						0.53	0.15						
47007.5540	OHP	−80.5						0.52	0.16						
47008.5020	OHP	−85.1						0.53	0.12						
47008.5190	OHP	−82.1						0.51	0.11						
47008.5240	OHP	−86.1						0.51	0.13						
47009.5260	OHP	−83.6						0.50	0.18						
47009.5380	OHP	−79.7						0.53	0.17						
47010.5490	OHP	−79.8						0.53	0.15						
47010.5580	OHP	−78.7						0.53	0.12						
47011.5540	OHP	−77.2						0.49	0.12						
47011.5610	OHP	−81.1						0.50	0.11						
47011.5680	OHP	−82.7						0.49	0.14						
47011.5720	OHP	−79.5						0.49	0.15						
47012.5660	OHP	−75.0						0.53	0.19						
47012.5730	OHP	−76.7						0.49	0.18						
47013.5400	OHP	−76.8						0.53	0.27						
47013.5450	OHP	−70.4						0.52	0.17						
47013.5490	OHP	−76.8						0.52	0.18						
47016.6010	OHP		−72.0	−68.6						0.13	−1.32				
48490.4780	OHP		−95.1							0.43	0.27				
48490.4890	OHP		−88.8							0.38	0.24				
48490.5050	OHP		−88.2							0.34	0.25				
48492.6390	OHP		−95.5							0.31	0.22				
48496.5900	OHP		−85.7							0.34	0.22				
48497.5810	OHP		−78.7							0.40	0.23				
49264.4470	OHP	−62.8						0.51	0.51						
49264.4520	OHP	−68.1						0.57	0.64						
49576.5530	OHP	−49.0						0.51	0.61						
49577.5420	OHP	−68.8						0.51	0.62						
49579.5220	OHP	−74.8						0.48	0.62						
49580.4810	OHP	−64.7						0.51	0.63						
49581.5350	OHP	−62.4						0.50	0.62						
49582.5110	OHP	−63.8						0.51	0.65						
49583.5330	OHP	−63.4						0.52	0.65						
50316.6500	OHP	−61.6	−66.6	−55.7	−82.8			0.53	0.78	0.40		0.19			
50316.6580	OHP	−68.2	−63.2	−56.9	−78.2			0.58	0.77	0.41		0.14			
50318.6440	OHP	−58.2	−64.0	−54.2	−80.5			0.52	0.79	0.43		0.23			
50506.2780	OHP													−5.39	−1.16
50507.2850	OHP													−5.56	−0.99
50508.2730	OHP													−5.17	−0.95
50510.2720	OHP													−5.27	−1.07
50638.5740	OHP	−68.1	−61.1	−55.6	−78.0			0.52	0.87	0.54		0.38			
50639.5570	OHP	−70.6	−58.7	−54.5	−74.4			0.55	0.77	0.53		0.39			
50642.5730	OHP	−66.3	−60.5	−53.1	−72.6			0.58	0.76	0.53		0.37			
51066.6350	OHP		−70.6	−67.1	−85.7					0.64					
51070.6290	OHP		−71.1	−66.5	−86.5					0.62					

Table A1 – *continued*

HJD-2400000	Obs.	RVs (km s⁻¹)						EWs (Å)							
		He II λ4200	He II λ4542	He II λ4686	N III	O III λ5592	C III λ5696	He II λ4200	Hγ	He I λ4471	Hβ	C III λ5696	He I λ5876	Hα	He I λ6678
51072.6380	OHP		−69.8	−63.1	−85.0					0.56					
51132.3770	OHP		−76.3		−90.8					0.75					
51132.4210	OHP		−72.2		−88.9					0.77					
51133.3300	OHP		−73.6		−87.8					0.74					
51133.3800	OHP		−73.6		−83.2					0.74					
51133.4320	OHP		−74.1		−90.2					0.74					
51133.5890	OHP		−73.5		−89.0					0.72					
51134.3780	OHP		−74.1		−90.3					0.68					
51134.4480	OHP		−71.9		−87.5					0.68					
51135.3390	OHP		−72.1		−84.7					0.72					
51135.3940	OHP		−74.2		−90.1					0.74					
51135.4580	OHP		−74.7		−93.4					0.70					
51136.3730	OHP		−72.0		−89.9					0.70					
51136.4390	OHP		−74.1		−90.4					0.65					
51137.4010	OHP		−73.2		−93.7					0.70					
51137.4670	OHP		−71.4		−94.8					0.73					
51374.5966	OHP	−78.8	−71.7	−69.0	−88.5			0.57	1.05	0.69	0.57				
51376.5322	OHP	−79.8	−76.4	−69.9	−90.7			0.62	1.14	0.76	0.66				
51378.5299	OHP	−78.0	−71.7	−67.0	−89.3			0.50	0.98	0.73	0.64				
51396.5996	OHP	−75.0	−72.7	−68.1	−86.8			0.47	1.11	0.80	0.65				
51403.6353	OHP	−76.0	−76.1	−70.4	−91.6			0.53	1.01	0.78	0.64				
51406.6338	OHP	−75.8	−75.1	−69.0	−90.9			0.57	1.07	0.77	0.60				
51407.6390	OHP	−76.4	−75.7	−69.9	−91.7			0.57	1.32	0.80	0.66				
51810.5860	OHP		−75.3	−68.2	−91.1					0.87	0.95				
51810.5950	OHP		−75.2	−70.0	−94.5					0.88	0.98				
51811.5670	OHP		−74.1	−68.2	−92.8					0.82	0.93				
51811.5750	OHP		−73.3	−68.2	−91.3					0.86	0.93				
51812.5940	OHP		−76.3	−71.4	−95.1					0.82	0.87				
51813.6030	OHP		−72.8	−65.8	−91.0					0.87	0.96				
51814.5950	OHP		−75.1	−67.3	−91.8					0.91	1.00				
51815.5960	OHP		−74.9	−70.2	−92.2					0.86	0.95				
51818.5310	OHP		−71.9	−65.8	−86.0					0.85	0.91				
51819.5600	OHP		−74.3	−68.0	−90.9					0.92	0.96				
51821.5610	OHP		−76.9	−71.2	−90.7					0.89	0.94				
52163.5010	OHP		−70.7	−68.4	−90.2					0.96	1.11				
52163.6530	OHP													−2.83	−0.32
52164.4950	OHP		−72.2	−68.2	−89.0					1.00	1.05				
52165.6280	OHP		−70.8	−67.2	−88.7					1.01	1.19				
52167.6240	OHP		−72.6	−66.4	−88.9					1.01	1.15				
52167.6530	OHP	−70.0						0.67	1.37						
52167.6670	OHP	−69.1						0.64	1.32						
52170.6510	OHP		−70.5	−67.3	−89.1					1.03	1.28				
52170.6650	OHP		−70.6	−66.7	−89.1					1.04	1.29				
52518.4763	OHP		−67.8	−63.2	−86.2					1.12	1.41				
52524.4224	OHP		−68.8	−66.1	−84.7					1.13	1.35				
52524.6509	OHP													−2.83	−0.12
52613.6360	OHP													−2.91	−0.35
52917.5310	OHP		−65.0	−64.5	−84.1					1.19	1.62				
52917.5410	OHP		−63.9	−62.2						1.32	1.50				
52918.5330	OHP		−66.7	−61.3	−82.3					1.14	1.59				
52918.5470	OHP		−63.9	−60.5	−78.1					1.17	1.68				
52919.3380	OHP													−1.54	0.06
52923.4040	OHP		−62.9	−63.3	−79.9					1.16	1.73				
53289.4940	OHP		−65.6	−59.6	−80.3					1.24	1.78				
53480.6160	OHP													−1.37	0.07
53548.5720	OHP		−61.8	−60.9	−77.0					1.26	1.89				
53549.5850	OHP													−0.83	0.21
53650.6420	OHP		−62.6	−57.2	−84.0					1.27	1.96				
53654.5800	OHP													−0.95	0.24
53775.2820	OHP					−67.9	−55.6					−0.73	2.06		
53776.2560	OHP					−73.2	−55.4					−0.56	1.91		
53778.2630	OHP					−71.0	−56.7					−0.66	2.13		

Table A1 – *continued*

HJD-2400000	Obs.	RVs (km s⁻¹) He II λ4200	He II λ4542	He II λ4686	N III	O III λ5592	C III λ5696	He II λ4200	EWs (Å) Hγ	He I λ4471	Hβ	C III λ5696	He I λ5876	Hα	He I λ6678
54389.3850	TBL	− 72.6	− 73.1	− 66.1		− 80.5	− 66.1		1.77	1.33	1.82	− 0.63	2.01	− 0.88	0.14
54389.4290	TBL	− 73.3	− 73.8	− 67.2		− 81.2	− 66.5		1.73	1.34	1.84	− 0.64	1.99	− 0.99	0.14
54389.4731	TBL	− 73.6	− 73.7	− 67.3		− 80.4	− 67.1		1.80	1.34	1.76	− 0.62	2.02	− 1.02	0.15
54390.4814	TBL	− 73.5	− 73.7	− 66.9		− 80.1	− 66.0		1.77	1.36	1.79	− 0.65	1.92	− 1.01	0.21
54390.5254	TBL	− 72.9	− 73.6	− 67.0		− 79.2	− 66.3		1.80	1.35	1.78	− 0.65	1.92	− 0.98	0.18
54390.5695	TBL	− 73.6	− 73.1	− 66.1		− 80.0	− 65.9		1.75	1.36	1.79	− 0.65	1.92	− 1.01	0.19
54392.3271	TBL	− 73.0	− 73.2	− 68.0		− 79.8	− 67.3		1.61	1.36	1.90	− 0.61	2.03	− 0.90	0.13
54392.3711	TBL	− 72.6	− 73.6	− 68.5		− 80.0	− 66.8		1.64	1.37	1.92	− 0.62	2.04	− 0.95	0.13
54392.4152	TBL	− 72.5	− 73.1	− 67.6		− 80.0	− 67.7		1.49	1.37	1.92	− 0.61	1.99	− 0.92	0.16
54393.3589	TBL	− 72.8	− 73.6	− 67.2		− 80.8	− 67.1		1.82	1.35	1.82	− 0.65	2.06	− 0.88	0.15
54393.4030	TBL	− 73.1	− 74.1	− 67.2		− 81.0	− 66.9		1.81	1.34	1.82	− 0.66	2.09	− 0.92	0.15
54393.4470	TBL	− 73.2	− 73.3	− 67.3		− 80.5	− 66.9		1.81	1.34	1.80	− 0.64	2.08	− 0.87	0.15
54394.3417	TBL	− 73.3	− 72.8	− 66.5		− 80.2	− 66.1		1.80	1.35	1.84	− 0.65	2.10	− 0.83	0.15
54394.3858	TBL	− 73.3	− 72.9	− 66.4		− 80.3	− 66.3		1.82	1.35	1.84	− 0.63	2.10	− 0.83	0.14
54394.4299	TBL	− 73.0	− 73.4	− 66.5		− 80.4	− 66.0		1.85	1.34	1.82	− 0.64	2.10	− 0.80	0.15
54395.3698	TBL	− 73.5	− 73.6	− 67.4		− 80.8	− 67.2					− 0.64	2.10		0.15
54395.4138	TBL	− 73.4	− 73.8	− 67.0		− 80.4	− 66.9		1.70	1.36	1.87	− 0.64	2.06	− 0.95	0.15
54395.4579	TBL	− 73.4	− 74.2			− 80.7	− 67.1								
54397.3470	TBL	− 72.0	− 73.2	− 67.9		− 80.2	− 67.2		1.79	1.35	1.87	− 0.65	2.01	− 0.84	0.21
54397.3911	TBL	− 72.6	− 73.4	− 68.7		− 79.8	− 66.8		1.83	1.37	1.88	− 0.64	2.04	− 0.80	0.22
54397.4352	TBL	− 72.4	− 72.9	− 68.1		− 80.0	− 66.7		1.86	1.35	1.87	− 0.65	2.03	− 0.81	0.25
54398.3486	TBL	− 72.4	− 73.2	− 67.7		− 80.0	− 66.8		1.82	1.35	1.84	− 0.62	2.05	− 0.85	0.19
54398.3927	TBL	− 73.1	− 73.3	− 67.3		− 80.1	− 66.7		1.83	1.35	1.83	− 0.62	2.03	− 0.88	0.18
54398.4368	TBL	− 73.2	− 73.0	− 67.1		− 79.9	− 67.1		1.79	1.35	1.78	− 0.63	2.03	− 0.91	0.17
54416.3270	OHP		− 70.0	− 67.7	− 86.6					1.28	1.85				
54416.3970	OHP		− 72.7	− 68.2	− 89.6					1.27	1.85				
54416.4760	OHP		− 70.9	− 66.5	− 87.0					1.27	1.86				
54416.6270	OHP		− 70.8	− 68.1	− 85.2					1.33	1.84				
54417.3600	OHP		− 67.2	− 62.5	− 81.2					1.32	1.89				
54418.3080	OHP		− 72.2	− 66.7	− 89.3					1.27	1.89				
54419.3800	OHP		− 72.1	− 67.7	− 90.1					1.27	1.91				
54472.2798	OHP					− 80.1	− 66.5					− 0.66	2.00		
54473.2353	OHP													− 1.07	0.15
54473.2513	OHP													− 1.19	0.16
54474.2838	OHP					− 81.7	− 68.7					− 0.62	2.05		
54475.2470	OHP					− 83.7	− 68.0					− 0.66	1.96		
54475.2679	OHP					− 82.3	− 67.6					− 0.65	1.94		
54711.6371	OHP		− 73.1	− 69.6	− 89.7					1.31	1.74				
54717.6173	OHP		− 72.6	− 69.8	− 88.9					1.27	1.82				
54718.6083	OHP		− 75.0	− 73.1	− 94.4					1.27	1.64				
54718.6228	OHP		− 77.0	− 74.0	− 90.8					1.25	1.71				
54740.5681	OHP		− 70.1	− 65.8	− 90.3					1.30	1.78				
54754.3051	TBL	− 73.9	− 74.5	− 69.5		− 80.7	− 68.0		1.72	1.32	1.73	− 0.66	1.88	− 1.07	0.09
54754.3492	TBL	− 74.7	− 74.7	− 68.7		− 81.3	− 67.6		1.76	1.32	1.70	− 0.66	1.88	− 1.03	0.09
54754.3932	TBL	− 74.5	− 74.5	− 69.0		− 81.8	− 67.8		1.78	1.32	1.70	− 0.67	1.89	− 1.06	0.09
54754.4372	TBL	− 73.6	− 73.9	− 70.3		− 80.9	− 67.5		1.73	1.32	1.67	− 0.67	1.88	− 1.11	0.10
54754.4813	TBL	− 73.4	− 73.9	− 69.4		− 81.2	− 67.7		1.74	1.32	1.68	− 0.67	1.88	− 1.16	0.08
54755.8528	CFHT	− 75.1	− 75.1	− 69.1		− 82.0	− 69.0	0.72	1.76	1.30	1.72	− 0.64	1.92	− 1.37	0.09
54755.8850	CFHT	− 74.6	− 74.6	− 69.7		− 82.5	− 68.8	0.69	1.78	1.30	1.71	− 0.65	1.91	− 1.36	0.12
54763.2869	TBL	− 74.4	− 74.9	− 68.9		− 82.3	− 67.9		1.70	1.31	1.75	− 0.64	1.91	− 1.14	0.10
54763.3309	TBL	− 75.3	− 75.8	− 69.6		− 82.1	− 67.9		1.72	1.31	1.71	− 0.63	1.87	− 1.16	0.09
54763.3750	TBL	− 74.5	− 75.4	− 69.1		− 82.3	− 68.1		1.73	1.31	1.75	− 0.66	1.89	− 1.19	0.10
54763.4191	TBL	− 74.8	− 75.2	− 68.9		− 82.7	− 68.2		1.68	1.32	1.69	− 0.64	1.86	− 1.21	0.12
54763.4631	TBL	− 74.4	− 75.5	− 69.0		− 81.6	− 67.9		1.67	1.33	1.78	− 0.63	1.85	− 1.19	0.12
54764.2673	TBL	− 74.7	− 74.2	− 69.3		− 82.2	− 68.1		1.76	1.34	1.74	− 0.67	1.89	− 1.12	0.11
54764.3113	TBL	− 73.8	− 74.7	− 68.5		− 81.9	− 67.9		1.76	1.34	1.73	− 0.67	1.88	− 1.13	0.11
54764.3554	TBL	− 74.2	− 74.4	− 68.5		− 82.1	− 67.9		1.82	1.33	1.72	− 0.67	1.90	− 1.13	0.11
54764.3994	TBL	− 74.7	− 75.1	− 69.1		− 82.2	− 67.9		1.80	1.34	1.73	− 0.67	1.91	− 1.15	0.10
54764.4435	TBL	− 75.1	− 75.0	− 69.0		− 82.3	− 67.7		1.81	1.33	1.72	− 0.68	1.91	− 1.13	0.10
54765.2791	TBL	− 74.6	− 75.3	− 68.4		− 82.7	− 68.4		1.75	1.35	1.76	− 0.65	2.01	− 1.14	0.08
54765.3231	TBL	− 74.2	− 74.8	− 69.4		− 82.5	− 68.4		1.76	1.34	1.76	− 0.65	2.01	− 1.10	0.06
54765.3672	TBL	− 74.5	− 74.2	− 69.5		− 81.0	− 68.4		1.70	1.35	1.81	− 0.64	1.99	− 1.10	0.04
54765.4113	TBL	− 74.2	− 74.4	− 68.6		− 81.8	− 68.1		1.61	1.34	1.82	− 0.64	1.98	− 1.02	0.06

Table A1 – *continued*

HJD-2400000	Obs.	RVs (km s⁻¹)							Hγ	EWs (Å)					
		He II λ4200	He II λ4542	He II λ4686	N III	O III λ5592	C III λ5696	He II λ4200		He I λ4471	Hβ	C III λ5696	He I λ5876	Hα	He I λ6678
54765.4553	TBL	−74.7	−75.6	−69.4		−81.6	−68.7		1.62	1.34	1.83	−0.65	1.98	−1.15	0.05
54766.2661	TBL	−74.6	−74.9	−69.1		−81.7	−68.9		1.62	1.31	1.76	−0.64	1.94	−1.14	0.08
54766.3101	TBL	−74.4	−75.0	−69.8		−82.0	−68.8		1.61	1.29	1.78	−0.65	1.90	−1.23	0.03
54766.3542	TBL	−74.5	−74.9	−68.9		−81.9	−68.5		1.63	1.30	1.79	−0.65	1.90	−1.20	0.02
54766.3983	TBL	−73.8	−74.4	−68.3		−81.5	−68.5		1.70	1.29	1.74	−0.64	1.92	−1.16	0.04
54766.4423	TBL	−74.1	−74.4	−69.1		−81.9	−68.9		1.70	1.30	1.75	−0.65	1.92	−1.17	0.06
54989.6730	OHP		−77.6	−72.3		−91.4	−74.9			1.39	1.71	−0.66	1.91	−1.29	
55018.0422	CFHT	−74.2	−73.3			−81.9	−67.1	0.70	1.72	1.27	1.73	−0.62	1.82	−1.33	0.07
55018.1049	CFHT	−73.4	−72.9			−81.8	−67.1	0.71	1.72	1.26		−0.62	1.83	−1.35	0.04
55020.0391	CFHT	−73.9	−74.1	−67.6		−82.4	−67.4	0.67	1.69	1.24		−0.64	1.86	−1.16	0.05
55020.1030	CFHT	−74.2	−73.7	−67.5		−81.3	−67.6	0.71	1.70	1.24		−0.63	1.88	−1.13	0.06
55022.0417	CFHT	−74.0	−73.5	−66.7		−80.6	−67.3	0.69	1.75	1.27		−0.64	1.82	−1.36	0.10
55022.1042	CFHT	−73.7	−73.2	−67.1		−81.7	−67.2	0.72	1.75	1.27	1.73	−0.64	1.83	−1.33	0.11
55026.0366	CFHT	−74.8	−73.9	−67.1		−82.8	−66.9	0.68	1.72	1.24		−0.64	1.91	−1.19	0.03
55026.1000	CFHT	−74.9	−74.1	−67.0		−82.6	−66.4	0.68	1.73	1.25	1.75	−0.65	1.93	−1.20	0.04
55027.0498	CFHT	−74.5	−74.2			−82.4	−67.2	0.69	1.71	1.24		−0.62	1.85	−1.31	0.11
55027.1125	CFHT	−74.2	−73.4			−82.1	−67.1	0.69	1.71	1.26		−0.62	1.84	−1.35	0.11
55033.5365	TBL	−74.4	−73.9	−70.1		−81.6	−66.9		1.44	1.32	1.70	−0.66	1.68	−1.45	0.12
55033.5961	TBL	−72.8	−73.0	−69.5		−81.4	−67.0		1.63	1.31	1.66	−0.66	1.74	−1.37	0.10
55033.6332	TBL	−73.0	−73.2	−69.2		−81.0	−67.5		1.69	1.30	1.63	−0.66	1.75	−1.28	0.11
55037.5291	TBL	−73.4	−73.4	−69.8		−81.2	−66.9		1.69	1.29	1.64	−0.63	1.85	−1.26	0.10
55037.5662	TBL	−73.8	−74.2	−69.8		−81.2	−67.0		1.74	1.29	1.64	−0.63	1.89	−1.24	0.10
55037.6033	TBL	−74.2	−74.1	−70.0		−81.6	−66.8		1.75	1.29	1.62	−0.62	1.89	−1.29	0.10
55038.5750	TBL	−72.8	−74.3	−71.8		−82.3	−67.3			1.30	1.77	−0.67	1.76	−1.29	0.07
55038.6098	TBL	−74.0	−74.2	−68.2		−81.1	−67.6			1.30	1.71	−0.66	1.80	−1.29	0.07
55038.6446	TBL	−73.2	−75.1	−67.9		−82.2	−67.8			1.28	1.66	−0.65	1.78	−1.30	0.06
55039.5371	TBL	−74.6	−74.3	−66.8		−81.8	−66.8			1.25	1.85	−0.68	1.68	−1.35	−0.01
55039.5768	TBL	−74.2	−73.7	−70.3		−81.3	−67.1			1.24	1.71	−0.67	1.71	−1.39	−0.01
55039.6165	TBL	−74.0	−74.4	−66.9		−81.2	−67.2			1.24	1.65	−0.65	1.75	−1.41	−0.01
55039.6562	TBL	−73.5	−74.0	−66.9		−81.9	−67.0			1.20	1.62	−0.65	1.75	−1.40	−0.03
55040.5356	TBL	−73.7	−74.8	−68.5		−82.6	−66.8			1.22	1.66	−0.65	1.64	−1.48	0.01
55040.5797	TBL	−73.9	−74.3	−67.7		−82.6	−66.7		1.45	1.21	1.64	−0.63	1.66	−1.41	−0.01
55040.6237	TBL	−74.0	−74.7	−68.5		−82.3	−66.7		1.49	1.20	1.54	−0.64	1.66	−1.46	0.01
55041.5277	TBL	−73.4	−73.6	−67.9		−82.1	−66.7		1.68	1.24	1.55	−0.65	1.78	−1.44	0.05
55041.5718	TBL	−73.8	−73.7	−68.0		−81.5	−66.4		1.71	1.25	1.55	−0.63	1.77	−1.44	0.06
55041.6158	TBL	−73.5	−73.7	−69.0		−81.6	−66.3		1.70	1.26	1.58	−0.64	1.75	−1.39	0.04
55042.5392	TBL	−73.7	−73.9	−68.9		−81.6	−67.0		1.77	1.28	1.61	−0.64	1.87	−1.16	0.10
55042.5832	TBL	−73.1	−73.8	−70.1		−81.2	−67.0		1.78	1.28	1.63	−0.64	1.88	−1.15	0.09
55042.6273	TBL	−73.4	−74.0	−69.8		−81.3	−67.0	0.81	1.74	1.28	1.66	−0.64	1.88	−1.19	0.09
55043.5212	TBL	−74.2	−74.1	−70.0		−82.1	−67.2		1.69	1.26	1.64	−0.63	1.81	−1.15	0.05
55043.5611	TBL	−74.0	−73.6	−70.3		−82.2	−67.4		1.69	1.26	1.64	−0.64		−1.11	0.04
55043.6011	TBL	−74.0	−74.0	−69.8		−82.1	−67.5		1.71	1.25	1.61	−0.63	1.84	−1.13	0.04
55043.6411	TBL	−73.7	−74.1	−70.6		−81.4	−67.1		1.69	1.25	1.64	−0.64	1.82	−1.13	0.05
55044.5389	TBL	−74.0	−74.0	−70.2		−80.9	−66.5		1.64	1.24	1.58	−0.67	1.69	−1.32	0.00
55044.5813	TBL	−73.7	−74.0	−68.9		−81.5	−66.5		1.68	1.23	1.55	−0.66	1.69	−1.29	−0.01
55044.6213	TBL	−73.7	−74.2	−68.5		−81.7	−66.5		1.70	1.23	1.57	−0.65	1.70	−1.28	0.00
55045.5349	TBL	−73.1	−74.2	−68.5		−81.9	−66.3			1.26	1.58	−0.64	1.70	−1.58	−0.02
55045.5790	TBL	−74.1	−74.6	−69.0		−82.3	−66.3			1.24	1.62	−0.65	1.69	−1.43	−0.01
55045.6232	TBL	−73.7	−74.0	−69.0		−82.5	−66.3			1.25	1.67	−0.65	1.68	−1.49	−0.02
55047.5158	TBL	−73.3	−74.0	−67.8		−81.7	−67.0			1.28	1.61	−0.66	1.67	−1.45	0.11
55047.5588	TBL	−73.4	−73.7	−69.5		−81.1	−67.0			1.28	1.60	−0.66	1.68	−1.49	0.11
55047.6029	TBL	−73.4	−73.9	−67.3		−81.3	−66.6			1.28	1.62	−0.66	1.68	−1.53	0.11
55047.6469	TBL	−73.4	−74.3	−67.9		−81.5	−67.1			1.29	1.64	−0.66	1.82	−1.25	0.06
55048.5598	TBL	−73.7	−74.2	−67.4		−82.1	−66.7		1.71	1.29	1.62	−0.67	1.81	−1.20	0.07
55048.6039	TBL	−73.0	−74.2	−68.5		−82.1	−66.7		1.70	1.29	1.66	−0.67	1.83	−1.17	0.06
55078.0702	CFHT	−73.5	−73.1			−81.7	−67.3	0.70	1.71	1.23	1.64	−0.63	1.80	−1.51	0.06
55082.9461	CFHT	−73.9	−73.7			−81.6	−67.3	0.74	1.82	1.28	1.78	−0.62	1.90	−1.23	0.13
55083.0085	CFHT	−73.6	−73.7			−81.9	−67.4	0.72	1.80	1.29	1.80	−0.62	1.91	−1.26	0.13
55099.8774	CFHT	−73.7	−73.7	−66.5		−81.1	−66.9	0.72	1.78	1.27	1.74	−0.65	1.87	−1.20	0.08
55099.9415	CFHT	−73.4	−73.2	−67.3		−80.8	−67.0	0.71	1.77	1.27		−0.65	1.86	−1.18	0.09
55105.8579	CFHT	−73.8	−73.0			−80.9	−67.0	0.72			1.61	−0.62	1.78	−1.62	0.09
55105.9207	CFHT	−73.5	−73.4			−80.9	−67.2	0.71				−0.62	1.76	−1.62	0.09

Table A1 – *continued*

HJD-2400000	Obs.	RVs (km s⁻¹)						EWs (Å)							
		He II $\lambda 4200$	He II $\lambda 4542$	He II $\lambda 4686$	N III	O III $\lambda 5592$	C III $\lambda 5696$	He II $\lambda 4200$	Hγ	He I $\lambda 4471$	Hβ	C III $\lambda 5696$	He I $\lambda 5876$	Hα	He I $\lambda 6678$
55109.9580	CFHT	−73.0	−72.7			−80.0	−66.7	0.72	1.70	1.25	1.67	−0.68	1.67	−1.45	0.05
55110.0211	CFHT	−73.0	−73.2			−80.6	−66.7	0.71	1.69	1.25	1.68	−0.69	1.62	−1.41	0.08
55114.8689	CFHT	−73.4	−73.1			−81.3	−67.0	0.74				−0.66	1.72	−1.44	0.03
55114.9320	CFHT	−73.5	−73.0			−81.1	−67.2	0.71		1.25		−0.66	1.73	−1.44	0.04
55175.2201	OHP		−71.9		−89.5					1.20					
55175.2410	OHP		−70.9		−87.5					1.19					
55177.4167	OHP		−72.0		−91.3					1.19					
55355.5903	OHP		−69.8	−66.1	−90.8					1.17		1.58			
55361.5958	OHP		−70.8	−66.6	−86.8					1.14		1.42			
55370.5972	OHP		−66.4		−87.0					1.13					
55373.6042	OHP		−66.6		−86.1					1.12					
55540.4047	OHP		−67.7		−85.2					1.05					
55541.4268	OHP		−68.6		−85.8					1.10					
55825.5705	OHP		−67.7		−84.9					1.00					
55825.5921	OHP		−68.2		−84.1					1.02					
55828.5075	OHP		−66.5		−82.8					1.02					
55828.5290	OHP		−66.6		−83.4					1.03					
55830.5096	OHP		−66.8		−84.1					1.03					
55830.5311	OHP		−67.9		−85.0					1.03					
56091.5878	OHP		−66.4		−80.8					0.85		0.91			
56093.5747	OHP		−62.3	−59.6	−79.8					0.90		1.03			
56093.5893	OHP		−64.9	−61.0	−80.1					0.91		1.01			
56094.5664	OHP		−66.4	−61.7	−81.0					0.88		0.95			
56094.5851	OHP		−65.2	−61.5	−83.7					0.86		0.95			
56095.5664	OHP		−64.3	−62.4	−80.8					0.87		0.97			
56095.5880	OHP		−64.0	−62.8	−80.8					0.88		0.96			
56096.5706	OHP		−63.1	−61.3	−78.5					0.92		0.91			
56096.5880	OHP		−63.4	−61.2	−78.3					0.88		0.98			
56456.5760	OHP		−60.9	−58.4	−82.7					0.85		0.87			
56456.5864	OHP		−61.7	−56.5	−73.3					0.84		0.84			
56457.5489	OHP		−61.1	−57.6	−78.6					0.81		0.77			
56457.5697	OHP		−63.0	−56.5	−80.9					0.77		0.76			
56458.5601	OHP		−60.5	−56.8	−80.2					0.79		0.77			
56458.5809	OHP		−59.4	−56.0	−77.3					0.81		0.76			
56459.5573	OHP		−59.9	−55.5	−82.0					0.85		0.82			
56459.5790	OHP		−60.3	−55.1	−77.5					0.86		0.80			
56460.5574	OHP		−59.0	−56.3	−75.8					0.86		0.93			
56460.5790	OHP		−59.2	−55.0	−77.4					0.86		0.88			
56514.8382	TIGRE	−66.8	−61.1	−62.9	−80.5	−80.0	−50.9	0.78	1.54	0.76	0.88		0.85	−4.11	−0.30
56519.7645	TIGRE	−61.4	−67.3	−61.8	−87.7	−78.5	−60.3	0.76	1.50	0.78	0.62		0.74	−3.92	−0.34
56533.7688	TIGRE	−62.9	−65.2	−60.9	−80.4	−78.1	−47.0	0.69	1.20	0.81	0.72		0.81	−3.91	−0.37
56561.7402	TIGRE	−61.9	−66.6	−62.8	−87.2	−65.0	−59.3	0.58	1.02	0.75	0.44		0.74	−3.62	−0.64
56568.7055	TIGRE	−62.2	−66.9	−59.0	−86.1	−69.5	−61.6	0.54	1.14	0.87	0.65		0.81	−3.78	−0.53
56580.6415	TIGRE	−64.9	−65.6	−61.3	−81.7	−69.7	−63.6	0.61	0.89	0.76	0.48		0.66	−4.06	−0.67
56581.7194	TIGRE	−62.1	−63.2	−59.4	−79.3	−78.9	−55.6	0.53	1.06	0.79	0.64		0.79	−4.00	−0.44
56584.7444	TIGRE	−60.7	−62.9	−62.3	−83.1	−67.1	−58.3	0.62	0.75	0.67	0.35		0.61	−4.10	−0.50
56590.7162	TIGRE	−67.5	−63.9	−62.4	−86.5		−55.4	0.64	1.07	0.80	0.60		0.78	−3.69	−0.55
56591.6544	TIGRE	−76.2	−73.8	−60.3	−85.6			0.52	0.89	0.70	1.00		0.88	−3.52	−0.57
56592.6282	TIGRE	−68.0	−66.2	−62.5	−86.7	−74.9	−60.3	0.75	1.05	0.63	0.20		0.37	−4.64	−0.85
56592.6378	TIGRE	−67.8	−63.9	−65.0	−77.9	−75.8		0.47	0.99	0.82	0.71		0.65	−3.47	−0.56
56592.7294	TIGRE	−67.4	−67.1	−62.5	−91.2	−83.7	−53.2	0.79	1.20	0.65	0.20		0.43	−4.59	−0.85
56604.6883	TIGRE	−67.2	−69.9	−62.3	−81.6	−69.7	−61.3	0.52	0.84	0.68	0.72		0.73	−3.78	−0.48
56640.5975	TIGRE	−69.9	−69.2	−62.3	−87.4	−77.9	−61.4	0.52	1.02	0.73	0.49		0.71	−3.93	−0.56
56643.5737	TIGRE	−69.6	−68.7	−64.3	−86.8	−77.7	−63.6	0.81	1.08	0.76	0.52		0.67	−4.03	−0.68
56644.5574	TIGRE	−73.1	−69.4	−67.1	−89.2	−74.8	−63.8	0.84	1.13	0.75	0.41		0.73	−3.97	−0.61
56645.5550	TIGRE	−64.1	−65.4	−60.5	−86.7	−77.1	−54.9	0.57	0.93	0.72	0.29		0.66	−4.07	−0.61
56646.5620	TIGRE	−67.1	−65.9	−59.5	−86.2	−75.3	−58.0	0.58	0.96	0.74	0.39		0.63	−4.07	−0.55
56813.9293	TIGRE	−65.8	−62.1	−60.9	−82.4			0.87	1.40	0.67	0.30		0.60	−4.34	−0.63
56818.9307	TIGRE												0.49	−4.10	−0.54
56819.9135	TIGRE	−65.3	−67.2	−66.8	−87.3			0.68	1.37	0.75	0.64		0.61	−3.72	−0.53
56860.9128	TIGRE	−65.4	−68.8	−59.9	−84.4			0.71	1.36	0.78	0.41		0.80	−4.44	−0.73
56861.8841	TIGRE	−72.6	−67.4	−59.9	−77.8			0.83	1.26	0.71	0.46		0.36	−4.76	−0.63
56863.9736	TIGRE	−66.5	−67.1	−58.6	−82.3	−78.0		0.64	1.40	0.66	0.33		0.57	−4.56	−0.45

Table A1 – *continued*

HJD-2400000	Obs.	He II λ4200	He II λ4542	He II λ4686	N III	O III λ5592	C III λ5696	He II λ4200	Hγ	He I λ4471	Hβ	C III λ5696	He I λ5876	Hα	He I λ6678
		\(RVs (km s^{-1})\)						\(EWs (Å)\)							
56867.8779	TIGRE	−67.8	−66.6	−59.8	−82.0	−80.4	−54.8	0.69	1.30	0.75	0.43		0.45	−4.54	−0.74
56895.9119	TIGRE	−65.8	−64.5	−60.2	−82.2	−76.0	−56.4	0.72	1.34	0.77	0.40		0.54	−4.77	−0.74
56897.9207	TIGRE	−65.3	−63.6	−62.6	−84.1	−72.5	−55.4	0.63	1.16	0.71	0.54		0.48	−4.57	−0.79
56907.8048	TIGRE	−68.7	−63.3	−60.3	−83.7	−77.7	−57.0	0.64	1.38	0.67	0.43		0.58	−4.42	−0.75
56910.8340	TIGRE	−67.6	−66.9	−61.6	−85.6	−75.4	−54.4	0.67	1.37	0.73	0.29		0.43	−4.71	−0.80
56920.7862	TIGRE	−66.3	−66.7	−62.9	−89.9	−70.6	−57.6	0.71	1.34	0.73	0.36		0.38	−4.57	−0.74
56939.7407	TIGRE	−69.0	−65.3	−62.5	−87.9	−74.1	−60.0	0.62	1.40	0.77	0.38		0.44	−4.87	−0.83
56940.7051	TIGRE	−68.3	−64.9	−63.4	−83.6	−73.9	−61.7	0.70	1.27	0.73	0.54		0.47	−4.58	−0.83
56941.6536	TIGRE	−68.0	−66.1	−61.8	−83.2	−71.7	−54.8	0.66	1.28	0.77	0.50		0.39	−4.66	−0.87
56953.6629	TIGRE	−65.3	−68.0	−64.1	−85.3	−63.0	−53.0	0.70	1.20	0.60	0.43		0.49	−4.43	−0.84
56954.5536	TIGRE	−73.6	−62.8	−62.8	−84.4			0.73	1.00	0.71	0.27		0.31	−4.79	−0.87
56956.6882	TIGRE	−67.8	−65.7	−62.9	−82.8	−69.4	−66.7	0.77	1.08	0.68	0.57		0.49	−4.59	−0.78
56957.6525	TIGRE	−68.0	−66.1	−62.3	−87.3	−71.5	−55.9	0.75	1.19	0.72	0.58		0.50	−4.71	−0.83
56959.6429	TIGRE	−66.4	−67.5	−63.1	−89.1	−73.1	−63.7	0.61	1.18	0.62	0.35		0.39	−4.64	−0.92
56960.6178	TIGRE	−66.4	−66.1	−63.2	−88.6	−73.4	−63.6	0.72	1.11	0.69	0.54		0.51	−4.70	−0.89
56960.7054	TIGRE	−65.4	−65.6	−61.9	−86.6	−72.1	−58.8	0.71	1.21	0.68	0.47		0.51	−4.63	−0.78
56961.8111	TIGRE	−67.4	−62.4	−61.8	−88.1	−66.1	−59.1	0.65	1.29	0.64	0.56		0.44	−4.60	−0.93
56965.6312	TIGRE	−65.0	−67.2	−63.0	−81.4			0.66	1.46	0.73	0.65		0.52	−4.79	−0.87
56971.7209	TIGRE	−66.2	−64.8	−60.6	−85.7	−74.6	−55.7	0.66	1.27	0.58	0.25		0.28	−4.85	−0.86
56974.6493	TIGRE	−68.6	−67.8	−61.9	−94.7		−60.5	0.66	1.29	0.69	0.32		0.44	−4.51	−0.87
56976.6454	TIGRE	−67.0	−66.0	−62.4	−87.9	−70.5	−61.2	0.63	1.19	0.64	0.41		0.39	−4.63	−0.88
56978.6015	TIGRE	−70.7	−67.2	−64.3	−91.2	−74.8	−63.1	0.64	1.32	0.70	0.42		0.42	−4.74	−0.76
56980.6470	TIGRE	−65.0	−65.4	−62.2	−89.6	−67.7	−58.6	0.61	1.21	0.70	0.49		0.54	−4.47	−0.87
56984.6739	TIGRE	−67.7	−66.1	−61.6	−84.1	−73.6	−58.1	0.68	1.36	0.66	0.34		0.36	−4.70	−0.78
56999.6410	TIGRE	−66.1	−63.9	−61.6	−84.8	−70.9	−60.9	0.60	1.40	0.70	0.52		0.55	−3.59	−0.58
57007.5755	TIGRE	−65.2	−64.3	−59.8	−85.9	−74.8	−59.1	0.64	1.35	0.72	0.45		0.46	−3.71	−0.59
57009.6294	TIGRE	−67.3	−64.6	−60.2	−85.6	−72.0	−61.7	0.66	1.39	0.76	0.56		0.44	−4.01	−0.62
57011.5726	TIGRE		−65.3	−60.5	−84.7	−75.7	−53.6		0.95	0.59	0.29		0.40	−3.73	−0.34
57013.6315	TIGRE	−67.0	−65.1	−63.8	−85.5	−73.1	−56.2	0.70	1.30	0.66	0.35		0.52	−3.70	−0.50
57015.5998	TIGRE	−68.7	−65.3	−62.2	−85.6	−69.1	−61.8	0.65	1.26	0.71	0.43		0.48	−3.88	−0.42
57231.9445	TIGRE	−73.4	−69.2	−66.8	−87.8	−74.7	−61.1	0.57	1.34	0.68	0.12		0.27	−5.46	−0.92
57268.9059	CFHT		−68.5	−64.1		−76.0	−62.0				0.24	−0.70	−0.05	−5.11	−1.00
57268.9681	CFHT		−68.6	−63.9		−76.8	−62.1				0.18	−0.69	−0.02	−5.17	−0.99
57286.7480	TIGRE	−70.6	−70.7	−66.1	−89.4	−79.7	−61.6	0.57	1.18	0.63	0.04		0.15	−5.69	−1.03
57293.8560	TIGRE	−70.5	−72.6	−66.7	−91.0	−78.8	−62.6	0.71	1.26	0.61	0.20		0.26	−5.25	−0.94
57294.8060	TIGRE	−71.9	−71.9	−65.9	−93.4	−78.3	−68.0	0.55	1.12	0.61	0.10		0.13	−5.71	−1.00
57297.8928	TIGRE	−70.0	−72.2	−66.7	−90.1	−80.3	−66.8	0.70	1.16	0.63	0.18		0.22	−5.57	−0.95
57298.7138	TIGRE	−72.6	−70.0	−66.6	−90.0	−79.6	−74.3	0.54	1.16	0.62	0.20		0.21	−5.53	−1.01
57298.8219	TIGRE	−71.8	−72.1	−66.3	−88.7	−79.0	−67.5	0.69	1.08	0.63	0.10		0.18	−5.62	−0.96
57299.7684	TIGRE	−71.1	−70.9	−64.8	−90.6	−78.7	−68.5	0.56	1.29	0.61	0.01		0.10	−5.66	−1.00
57300.7475	TIGRE	−69.5	−72.5	−66.4	−95.5	−76.5	−69.4	0.64	1.32	0.62	0.17		0.13	−5.33	−1.10
57304.6782	TIGRE	−70.1	−73.4	−67.1	−93.5	−76.9		0.63	1.08	0.61	0.21		0.13	−5.48	−0.90
57304.7608	TIGRE	−69.9	−73.1	−65.7	−90.1	−79.2	−65.4	0.71	1.26	0.63	0.08		0.13	−5.57	−0.91
57307.7435	TIGRE	−68.8	−69.3	−66.1	−89.5	−80.1	−62.3	0.74	1.27	0.55	0.27		0.23	−5.52	−0.98
57310.6171	TIGRE	−73.9	−70.0	−66.4	−91.3	−81.6	−63.9	0.64	1.37	0.71	0.23		0.20	−5.08	−0.96
57310.7595	TIGRE	−71.9	−70.9	−67.0	−93.8	−76.2	−65.0	0.63	1.13	0.64	0.30		0.27	−5.14	−1.02
57315.6104	TIGRE	−72.6	−72.1	−67.8	−90.5	−79.6	−67.6	0.69	1.15	0.69	0.09		0.12	−5.79	−0.96
57315.7346	TIGRE	−72.4	−70.0	−66.4	−91.6	−79.6	−63.6	0.71	1.15	0.62	0.05		0.13	−5.77	−0.95
57316.6673	TIGRE	−74.8	−70.3	−66.0	−91.2	−80.9	−67.1	0.66	1.08	0.62	0.09		0.21	−5.47	−0.98
57317.6686	TIGRE	−70.1	−69.8	−67.4	−92.2			0.68	1.27	0.70	0.10		0.11	−5.29	−1.11
57320.7903	TIGRE	−70.4	−70.5	−66.3	−89.9	−76.5	−61.3	0.68	1.32	0.59	0.06		0.22	−5.43	−0.94
57330.7925	TIGRE	−72.0	−71.0	−67.7	−91.1		−65.8	0.53	1.25	0.58	0.10		0.15	−5.43	−1.05
57332.6559	TIGRE	−72.9	−71.2	−68.5	−93.3	−81.4	−64.4	0.60	1.18	0.60	0.15		0.12	−5.33	−1.11
57334.6326	TIGRE	−73.9	−72.6	−67.2	−91.1			0.60	1.23	0.56	0.33		0.17	−5.41	−1.08
57336.6533	TIGRE	−71.8	−72.4	−68.9	−90.9	−82.4	−66.7	0.54	1.09	0.56	0.18		0.16	−5.39	−1.15
57338.5743	TIGRE	−71.3	−71.6	−67.4	−92.3	−79.6	−65.8	0.63	1.09	0.60	0.19		0.16	−5.60	−1.10
57973.8502	TIGRE	−75.7	−76.9	−75.0	−95.1	−85.2	−67.6	0.69	0.80	0.45	−0.44		−0.24	−6.35	−1.20
58002.6230	OHP		−77.8	−73.2	−93.8					0.44	−0.31				
58002.6342	OHP		−77.1	−72.4	−93.0					0.48	−0.21				
58003.6318	OHP		−73.0	−68.2	−90.6					0.44	−0.21				
58006.6250	OHP		−75.1	−69.6	−91.9					0.49	−0.27				
58275.9330	TIGRE	−74.7	−74.4	−70.0	−93.6	−84.8	−65.2	0.55	0.41	0.38	−0.61		−0.42	−7.08	−1.45

Table A1 – *continued*

| HJD-2400000 | Obs. | RVs (km s⁻¹) | | | | | | | | EWs (Å) | | | | | |
---	---	He II λ4200	He II λ4542	He II λ4686	N III	O III λ5592	C III λ5696	He II λ4200	Hγ	He I λ4471	Hβ	C III λ5696	He I λ5876	Hα	He I λ6678
58318.9006	TIGRE	−78.7	−76.8	−72.5	−91.6	−81.4	−71.5	0.70	0.83	0.46	−0.70		−0.41	−7.39	−1.29
58352.6205	OHP		−73.5	−66.3	−91.9					0.36	−0.53				
58353.6255	OHP		−73.6	−68.5	−91.8					0.39	−0.36				
58357.6083	OHP		−76.4	−70.7	−92.3					0.40	−0.42				
58357.6222	OHP		−74.3	−72.4	−90.7					0.39	−0.47				
58636.9404	TIGRE	−74.6	−72.9	−69.2	−90.6	−80.8	−63.4	0.56	0.37	0.32	−0.82		−0.58	−7.60	−1.42
58721.5006	OHP		−71.0	−66.0	−83.2					0.35	−0.64				
58721.5219	OHP		−68.8	−65.2	−87.9					0.34	−0.65				
58722.4960	OHP		−69.3	−63.5	−85.5					0.35	−0.62				
58806.8216	CFHT	−70.5	−70.2			−78.4	−64.6			0.32		−0.63	−0.85	−8.14	−1.55
59048.9064	TIGRE	−71.3	−70.4	−63.9	−89.0	−81.6	−60.8	0.62	0.51	0.33	−1.31		−0.88	−8.66	−1.53
59118.5307	OHP													−8.69	−1.61
59118.5522	OHP													−8.86	−1.64
59119.5186	OHP													−8.83	−1.63
59119.5333	OHP													−8.93	−1.54
59121.5190	OHP													−8.60	−1.54
59121.5330	OHP													−8.94	−1.52
59122.5132	OHP													−8.72	−1.52
59122.5272	OHP													−8.09	−1.47
59493.5495	OHP													−9.40	−1.69
59493.5672	OHP													−9.45	−1.65
59493.5890	OHP													−9.51	−1.75
59495.5233	OHP													−9.28	−1.73
59495.5341	OHP													−9.26	−1.68
59495.5446	OHP													−9.19	−1.70
59496.4551	OHP													−9.50	−1.70
59496.4656	OHP													−9.43	−1.71
59496.4762	OHP													−9.39	−1.73
59496.4867	OHP													−9.46	−1.68
59496.4974	OHP													−9.42	−1.74
59498.4893	OHP													−9.33	−1.72
59498.5035	OHP													−9.25	−1.65
59498.5175	OHP													−9.46	−1.67
59498.5318	OHP													−9.40	−1.68
59498.7516	TIGRE	−67.8	−67.2	−62.4	−85.2	−74.4	−58.5	0.69	0.47	0.28	−1.36		−1.15	−9.39	−1.86
59552.5563	TIGRE	−67.9	−65.6	−60.0	−85.1	−72.5	−59.6	0.69	0.25	0.20	−1.35		−1.02	−9.18	−1.77
59564.6448	TIGRE	−65.3	−65.3	−62.3	−88.1	−71.4	−61.3	0.57	0.29	0.20	−1.26		−1.13	−9.41	−1.87
59570.5869	TIGRE	−66.7	−65.8	−59.7	−83.4	−73.7	−67.6	0.72	0.34	0.25	−1.41		−1.08	−9.52	−1.84
59811.8731	TIGRE	−65.2	−62.1	−56.3	−78.3	−70.3	−54.7	0.75	0.43	0.18	−1.64		−1.21	−10.12	−1.65
59814.8401	TIGRE	−65.8	−62.5	−59.8	−83.2	−69.3	−56.3	0.82	0.46	0.22	−1.53		−1.16	−9.85	−1.60
59851.5520	OHP		−61.5	−60.3	−81.3					0.16	−1.18				
59851.5690	OHP		−59.3	−54.3	−78.7					0.22	−1.14				
59852.5420	OHP		−56.9	−53.6	−76.0					0.21	−1.22				
59852.5630	OHP		−56.4	−54.5	−75.3					0.18	−1.20				
59855.5060	OHP		−60.4	−57.3	−74.5					0.17	−1.19				
59855.5220	OHP		−61.0	−57.3	−78.6					0.18	−1.18				
59855.5500	OHP		−59.7	−58.4	−79.2					0.20	−1.15				
59855.5790	OHP		−58.5	−56.3	−80.2					0.18	−1.27				
59855.6070	OHP		−56.7	−55.0	−78.3					0.17	−1.13				
59855.6360	OHP		−61.0	−54.6	−79.1					0.19	−1.18				
59855.6610	OHP		−59.7	−55.2	−83.7					0.15	−1.18				
59951.6041	TIGRE	−60.7	−62.5	−59.7	−83.3	−69.6	−58.1	0.52	0.01	0.15	−1.54	−0.33	−1.34	−10.12	−1.80

This paper has been typeset from a TEX/LATEX file prepared by the author.